






RESEARCH ARTICLE

The effects of biomass depth distribution on phytoplankton spring bloom dynamics and composition in an Arctic fjord

Clara J. M. Hoppe^{1,*} , Klara K. E. Wolf^{1,2} , F. Cottier^{3,4} , E. Leu⁵ , M. Maturilli⁶ , and B. Rost^{1,7} 

Fjord systems are among the most productive and best described of Arctic marine habitats. Contributing substantially to that overall productivity, spring phytoplankton blooms are one of the most important features of fjord systems and of mid- and high-latitude oceans in general. Understanding specific mechanisms that control the timing, magnitude, and composition of these blooms is among the most central, and yet unresolved, questions within biological oceanography. To elucidate how the distribution of phytoplankton with depth affects bloom dynamics, we analyzed a comprehensive dataset on spring blooms in an Arctic fjord from three consecutive years, covering environmental drivers as well as ecological and biogeochemical dynamics. Our data show that the build-up of biomass correlated positively with the chlorophyll layer depth (CLD, defined as the depth at the bottom of the layer containing a threshold concentration of chlorophyll *a*), with highest rates of biomass accumulation occurring in more depth-extended distributions despite lower light availability at greater depths. Based on our results, we hypothesize that this relationship is caused by reduced grazing pressure under conditions of deepening mixing layers. Further, we postulate that changes in the depth to which phytoplankton biomass is distributed have the potential to control the species composition of the Arctic phytoplankton spring bloom, with diatoms dominating in situations with shallow CLDs and *Phaeocystis pouchetii* with deepening CLDs, which may impact the biogeochemistry of the studied fjord system differently.

Keywords: Svalbard, *Phaeocystis*, Diatoms, Primary production, Grazing pressure, Kongsfjorden

1. Introduction

Primary production by phytoplankton represents the base of pelagic food webs and strongly influences biogeochemical cycles (Falkowski et al., 1998). Especially in high latitude areas with strong seasonality, the mass accumulation of phototrophic biomass during the spring phytoplankton bloom plays a central role for marine ecosystems (Assmy and Smetacek, 2009), with coastal areas being most productive (Carmack and Wassmann, 2006; Ardyna et al., 2017). A better understanding about controlling drivers of primary production and phytoplankton bloom

dynamics is needed for modeling potential climate change effects on ecosystem functioning (Constable et al., 2022). The most important bottom-up controlling factors for primary production and growth are light and nutrient availability. Phytoplankton biomass accumulation and bloom formation are determined by the subsequent gains together with losses that occur due to grazing, viral lysis, and sinking.

How phytoplankton are distributed in the water column affects all of these controlling factors. Most fundamentally, due to the attenuation of photosynthetically active radiation (PAR) with depth, the depth distribution of phytoplankton determines the light energy that cells have available for photosynthesis and net growth (Jassby and Platt, 1976). In addition to the total daily irradiance dose as a function of depth, active deepening or shoaling of the mixing layer depth also determines the variability of light exposure (MacIntyre et al., 2000), with strong impacts on physiology and growth (Hoppe et al., 2015; White et al., 2020). Water column stability and subsequent depth distribution also affect phytoplankton via their effects on nutrient availability. The shallower the surface mixed layer, the faster the nutrients needed for biomass build-up are being depleted for the same

¹ Alfred-Wegener-Institut Helmholtz-Zentrum für Polar- und Meeresforschung, Bremerhaven, Germany

² Limnological Institute, University of Konstanz, Mainaustraße, Konstanz, Germany

³ Scottish Marine Institute, Oban, UK

⁴ UiT The Arctic University of Norway, Tromsø, Norway

⁵ Akvaplan-niva, Fram Center, Tromsø, Norway

⁶ Alfred-Wegener-Institut Helmholtz-Zentrum für Polar- und Meeresforschung, Potsdam, Germany

⁷ University of Bremen, Bremen, Germany

* Corresponding author:
Email: clara.hoppe@awi.de

standing stock size. Consequently, strongly stratified systems such as Arctic waters often exhibit subsurface chlorophyll *a* (Chl *a*) maxima below the mixed layer, where nutrients are not yet depleted (Cornec et al., 2021). Episodic mixing events, for example, via storms, entrain nutrients into the previously stratified nutrient-limited surface waters and enable, for example, the formation of fall blooms (Ardyna et al., 2014). Importantly, changes in the depth distribution of phytoplankton can also alleviate grazing pressure and viral attack rates, as prey encounter rates decrease with dilution of the upper water column, allowing a transient decoupling between prey and predator biomass (Behrenfeld and Boss, 2018).

The depth distribution of phytoplankton itself is driven by two fundamentally different mechanisms. On the one hand, ocean turbulence, for example, due to wind-driven mixing, affects the depth distribution of phytoplankton via active mixing (Brainerd and Gregg, 1995), with deepening active mixing depths also causing a deeper distribution of biomass within the water column (Huisman et al., 1999). The active mixing depth, that is, the depth to which turbulent mixing takes place at a certain point in time, is important to distinguish from the classical mixed layer depth (MLD), which describes the depth of uniform surface temperature and salinity (Franks, 2015). A past active mixing event can have created a certain MLD, while the current active turbulent mixing penetrates less deeply in the water column, and thus only vertically redistributes properties and particles in this shallower layer, which is invisible to the classical MLD definition. The depth distribution of phytoplankton can therefore be influenced by several past mixing events, for example, with an actively mixed surface community and several layers of biomass from re-stabilized, previous deeper mixing layers.

On the other hand, increasing or decreasing rates of net biomass build-up will change the phytoplankton biomass within a certain layer, depending on the specific bottom-up (light and nutrient) and top-down (grazing) effects at this depth. Further, biomass can sink from the surface ocean and also be re-entrained to the surface from below the active mixing layer under intensified mixing. Importantly, the degree to which phytoplankton biomass build-up dominates the depth distribution of phytoplankton depends on the frequency and duration of environmental dynamics (Carranza et al., 2018). Especially in weakly stratified systems such as Arctic fjords in spring (Cottier et al., 2010; Inall et al., 2015), the depth distribution of biomass (described as the chlorophyll layer depth, CLD, in this study) therefore does not necessarily reflect MLD, but instead the past dynamics of the active mixing depth.

Representing a well-studied Arctic coastal site, Kongsfjorden on the western coast of Svalbard (79°N; **Figure 1**) is a highly productive fjord system that exhibits a classical spring bloom-dominated phenology (Hegseth et al., 2019). Located in an Arctic area of unprecedented climate change, Kongsfjorden may serve as a model system to study the changes to be anticipated in other Arctic systems (Bischof et al., 2019). Kongsfjorden surface waters have warmed by about 1.3°C per decade since 2002, mainly due to increased inflow of warmer Atlantic water

masses, with particularly pronounced warming in winter and early spring (Cottier et al., 2019; Tverberg et al., 2019). Due to these conditions, the fjord typically no longer exhibits a sea ice cover, with winter and spring fast ice being restricted to the shallowest areas of the inner fjord (Pavlova et al., 2019; Gerland et al., 2020). In contrast to the open ocean, which consistently possesses a pycnocline at some depth, high latitude fjords are characterized by full-depth mixing of the water column due to both thermal and haline convection (Cottier et al., 2010), which is most pronounced in winter. In spring, Kongsfjorden therefore does not exhibit a classical pycnocline (Inall et al., 2015). Restratification occurs only after the spring bloom (Inall et al., 2015) and is dominated by the input of fresh-water from surface runoff and glacial discharges in summer (Cottier et al., 2010; Tverberg et al., 2019).

Phytoplankton spring blooms in Kongsfjorden usually occur between April and June, and are initiated when days become longer and weather stabilizes after deep mixing in winter has replenished the nutrient pools in surface waters. The specific timing of Kongsfjorden spring blooms is thought to be controlled by various environmental drivers such as irradiance, nutrients, advection, and stratification, with eased light limitation after the end of the polar night being the main driver for bloom development (Hegseth et al., 2019; Singh et al., 2020; van de Poll et al., 2020). The timing and intensity of the Kongsfjorden spring bloom is also thought to depend on the availability of “seeding populations” in the water column and surface sediments (Hegseth and Tverberg, 2013; Hegseth et al., 2019). In coastal regions, many of the common genera of Arctic bloom-forming diatoms (e.g., *Thalassiosira*, *Chaetoceros*) are known to form resting stages that overwinter in the surface sediment until they germinate and are transported back to the surface by deep mixing in early spring (McQuoid and Hobson, 1996; Hegseth and Tverberg, 2013; Hegseth et al., 2019). Increasing evidence suggests, however, that a large fraction of phototrophs survive as active cells in the water column around Svalbard, with the return of the sun after the polar night setting the earliest limit for the re-initiation of primary production (Berge et al., 2015; Vader et al., 2015; Kvernvik et al., 2018; Hoppe, 2022).

Similar to other coastal Arctic regions, spring blooms in Kongsfjorden are usually dominated by either diatoms or *Phaeocystis* (Hegseth et al., 2019; Assmy et al., 2023). Due to their different roles for Arctic ecosystem functioning, underlying mechanisms of their relative dominance have been subject to many studies (Degerlund and Eilertsen, 2009; Hegseth and Tverberg, 2013; Assmy et al., 2017; Hegseth et al., 2019). While *Phaeocystis pouchetii* and *P. globosa* are sometimes used as indicators for Atlantification (Hegseth and Tverberg, 2013; Bischof et al., 2019; Orkney et al., 2020), that is, the intrusion and establishment of temperate species in the Atlantic sector of the Arctic Ocean, this genus has always occurred in and significantly contributed to Arctic phytoplankton assemblages (Hsiao, 1980; Hasle and Heimdal, 1998; von Quillfeldt, 2000). Traditionally, the genus *Phaeocystis* is considered important under low silicate concentrations

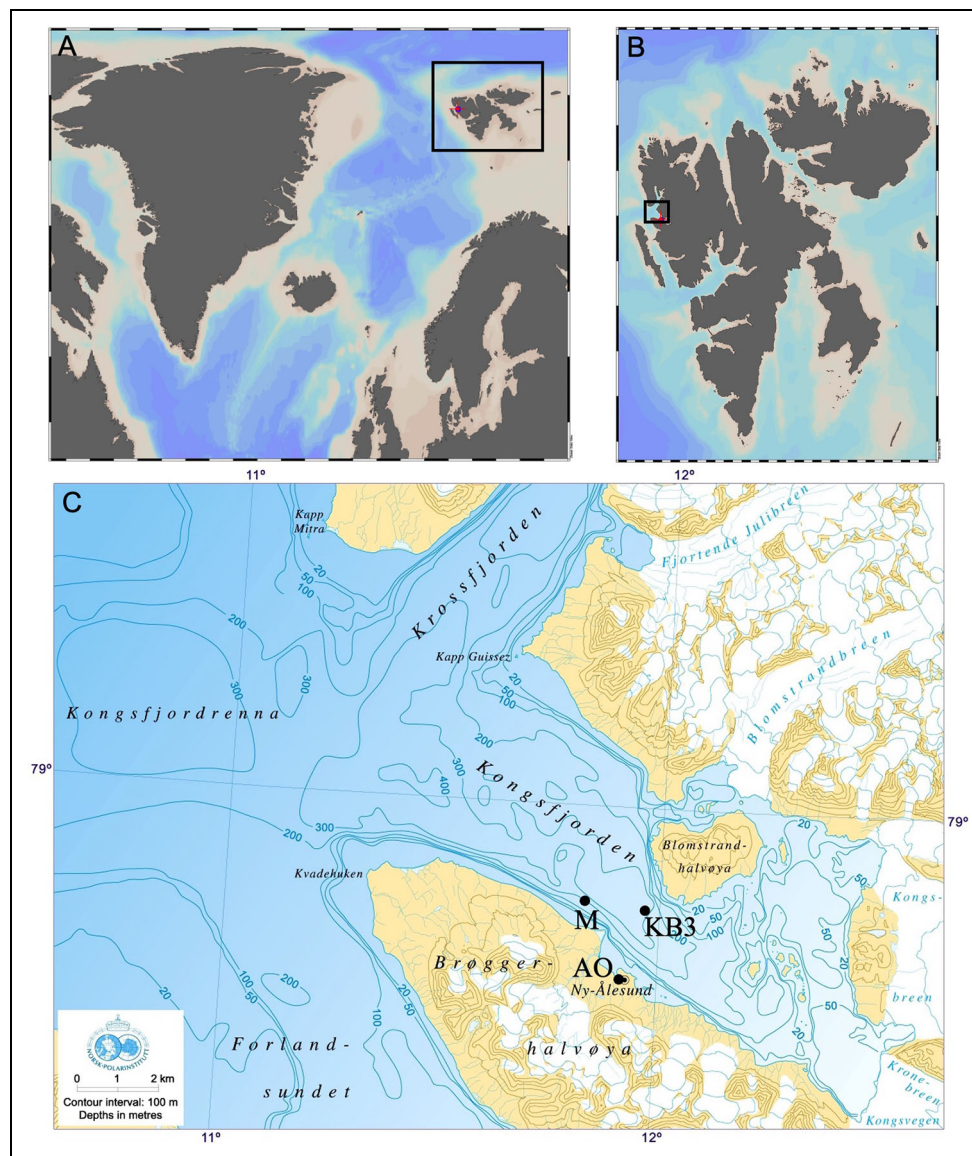


Figure 1. Map showing the sampling locations of this study. (A) Location of Svalbard in the European Arctic, (B) Kongfjorden on Svalbard's west coast, and (C) the three study locations within the fjord: sampling site KB3, mooring location M, and AWIPEV Atmospheric Observatory AO. Overview maps (A and B) were derived from Ocean Data View; detailed marine topographical map (C) was provided by the Norwegian Polar Institute.

or high nitrate-to-silicate ratios such as during the later stage of Arctic spring blooms, that is, following diatoms in the species succession (Leu et al., 2006; Hodal et al., 2012; Hegseth et al., 2019; Ardyna and Arrigo, 2020). Recently, the number of observations of large-scale *Phaeocystis* blooms that are not necessarily connected to an earlier diatom peak has increased (Nöthig et al., 2015; Assmy et al., 2017; Ardyna et al., 2020; Assmy et al., 2023). These blooms have been identified to occur especially under low irradiance conditions imposed by snow and ice cover (Assmy et al., 2017) or in deep mixed layers (Reigstad et al., 2002; Degerlund and Eilertsen, 2009). No real consensus on the grazing on *Phaeocystis* exists to date, although most authors agree that grazing control on *Phaeocystis* is lower than that on diatoms. This lower grazing control can be attributed in part to the ability of *Phaeocystis* to “escape” grazers by dramatically altering its

size via colony formation (Hamm and Rousseau, 2003; Wassmann et al., 2005; Nejstgaard et al., 2007; Ray et al., 2016). Large colonies most likely can only be grazed upon by larger zooplankton, such as calanoid copepods and krill, but not by smaller zooplankton (Hamm et al., 2001; Nejstgaard et al., 2007). *Phaeocystis*-dominated and diatom-dominated blooms also exhibit fundamentally different biogeochemical characteristics and export dynamics. While *Phaeocystis* can significantly contribute to carbon drawdown, the majority of studies show strongly reduced sedimentation and carbon export compared to diatom-dominated systems (Rousseau et al., 2000; Reigstad and Wassmann, 2007; Wolf et al., 2016; Wiedmann et al., 2020).

In this process study, we investigated the phytoplankton dynamics of spring blooms in Kongfjorden over three consecutive years (2016–2018). We focused on the relative

importance of various environmental drivers and how they may affect various biological parameters such as biomass build-up and species dominance. The aim of this study was to disentangle the roles of different controlling factors and to evaluate the role of biomass depth distribution for bloom dynamics and composition during the three studied spring periods.

2. Methods

2.1. Sampling location

Regular sampling was conducted in April and May 2016–2018 in Kongsfjorden, Svalbard (**Figure 1**). Kongsfjorden is an open fjord, approximately 25 km long on the west coast of the island, which is characterized by periodic advection of water masses from Fram Strait as well as freshwater input from several large tidewater glaciers and rivers (Tverberg et al., 2019). The sampling station KB3 (78°57.22'N, 11°57.44'E; **Figure 1C**) is located in the center of the fjord. With a depth of 330 m, it is one of the deepest locations in this part of the fjord, not directly influenced by the river and glacier plumes, but potentially affected by advection from the west.

2.2. Sensor-derived hydrographic and Chl *a* data

Hydrographic data were collected with a XR-620 CTD (RBR Ltd, Ottawa, Canada), equipped with a fluorescence sensor, which was deployed to 100 m depth at station KB3 (78°57.18'N, 11°57.23'E, 329 m water depth) during each sampling event. Potential density was estimated from CTD profiles, and the difference in potential density between data from 2 m and 95 m was calculated to investigate stratification. Different MLD calculations were compared as described in detail in Text S1 (Figure S1). Due to weather restrictions for sampling from open boats used for this study, our CTD profiles may be biased toward calmer days. Measured CLDs, however, represent depth distribution from current and previous mixing events.

In addition, continuous temperature and salinity data were collected from a mooring (Hop et al., 2019) located less than 3 nautical miles from KB3 (78°57.4'N, 11°49.6'E, 230 m water depth). Temperature was measured at a series of depth levels using Seabird instrumentation (SBE56, SBE37, and SBE16+, Sea-Bird Scientific, Bellevue, WA). The sensors were deployed after factory calibration and quality-checked after recovery. The temperature measurements were made at a resolution of 0.01°C or greater and accurate to at least 0.1°C. Data were interpolated onto a regularly spaced grid of 1-hour time intervals and 10 m depth intervals and then low-pass-filtered to remove tidal oscillations that would mask temporal signals (Thompson, 1983). Salinity was derived from measurements of conductivity from either pumped Seabird 37 or Seabird 16+ units (Sea-Bird Scientific, Bellevue, WA). Data were despiked, and no significant drift of the sensors was noted.

Fluorescence-derived Chl *a* concentrations ($\mu\text{g L}^{-1}$) from CTD casts were corrected based on discrete Chl *a* samples for each year (Pearson's *r* linear regression between both estimates: in 2016, $n = 40$, $r^2 = 0.81$, $p < 0.0001$; in 2017, $n = 37$, $r^2 = 0.86$, $p < 0.0001$; in 2018, $n = 39$, $r^2 = 0.81$, $p < 0.0001$). An underestimation of

surface Chl *a* concentrations due to fluorescence quenching by high actinic irradiances was corrected following Xing et al. (2012). In short, maximal Chl *a* concentrations measured in the uppermost active mixing layer were projected to the surface. Depth-integrated Chl *a* concentrations (0–100 m) in the upper water column were calculated via numerical integration. In cases where CTD profiles did not reach full 100 m (by up to 7 m), the average of the last 5 m was projected to 100 m.

Bloom phases were defined based on changes in depth-integrated Chl *a*, via calculating the rate of change between sampling dates, dx/dt (i.e., $[\text{Chl } a_1 - \text{Chl } a_0]/[t_1 - t_0]$), in depth-integrated Chl *a* that was previously normalized to the maximum Chl *a* inventory per year. The main bloom phase was identified as the period between the first and last time point per year with a rate of change in normalized depth-integrated Chl *a* inventories (i.e., dx/dt) > 0.05 . The pre-climax phase (not termed pre-bloom as this occurred prior to the start of the sampling campaigns when biomass was already increasing) and the post-bloom phase describe the periods before and after the main phase, respectively (**Table 1**). Gaps between defined phases originate from time periods between sampling events.

We define the chlorophyll layer depth (CLD) as the depth at the bottom of the layer that contained more than $2.5 \mu\text{g Chl } a \text{ L}^{-1}$, a threshold that relatively reliably represents the lower level of the depth distribution for main bloom periods in the presented dataset (**Figure 2**). In cases with Chl *a* concentrations remaining high (i.e., above the threshold) over the entire measured depth of the profile, the corresponding CLD was set to 100 m, even though the actual CLD was probably deeper than the maximal depths at which data were collected (as indicated by writing $> 100 \text{ m}$).

2.3. Wind, irradiance measurements and light field simulations

Average wind speed and direction as well as incoming incident PAR were measured close to the nearby AWIPEV Atmospheric Observatory (Maturilli, 2020a). In short, a combined classic wind sensor (ThiesClima, Göttingen, Germany) was used to derive hourly averaged wind speed (m s^{-1}) and direction ($^\circ$) that were recorded at 10 m height. Hourly averaged (from measurements conducted every minute)

Table 1. Timing of bloom phases for the three years studied

Year	Bloom Phases ^a		
	Pre-climax	Main Bloom	Post-apex
2016	Apr 8–16	Apr 21–May 16	May 19–30
2017	Apr 12–20	Apr 24–May 4	May 11–26
2018	Apr 10–25	Apr 27–May 11	May 14–22

^aThe main phase was identified based on normalized rate of change in depth-integrated Chl *a* inventories > 0.05 for the first and last timepoints per year. Pre-climax and post-bloom phases are the periods before and after the main bloom phase. Gaps between phases originate from the lack of data due to non-daily sampling during these time periods (usually 2–4 days).

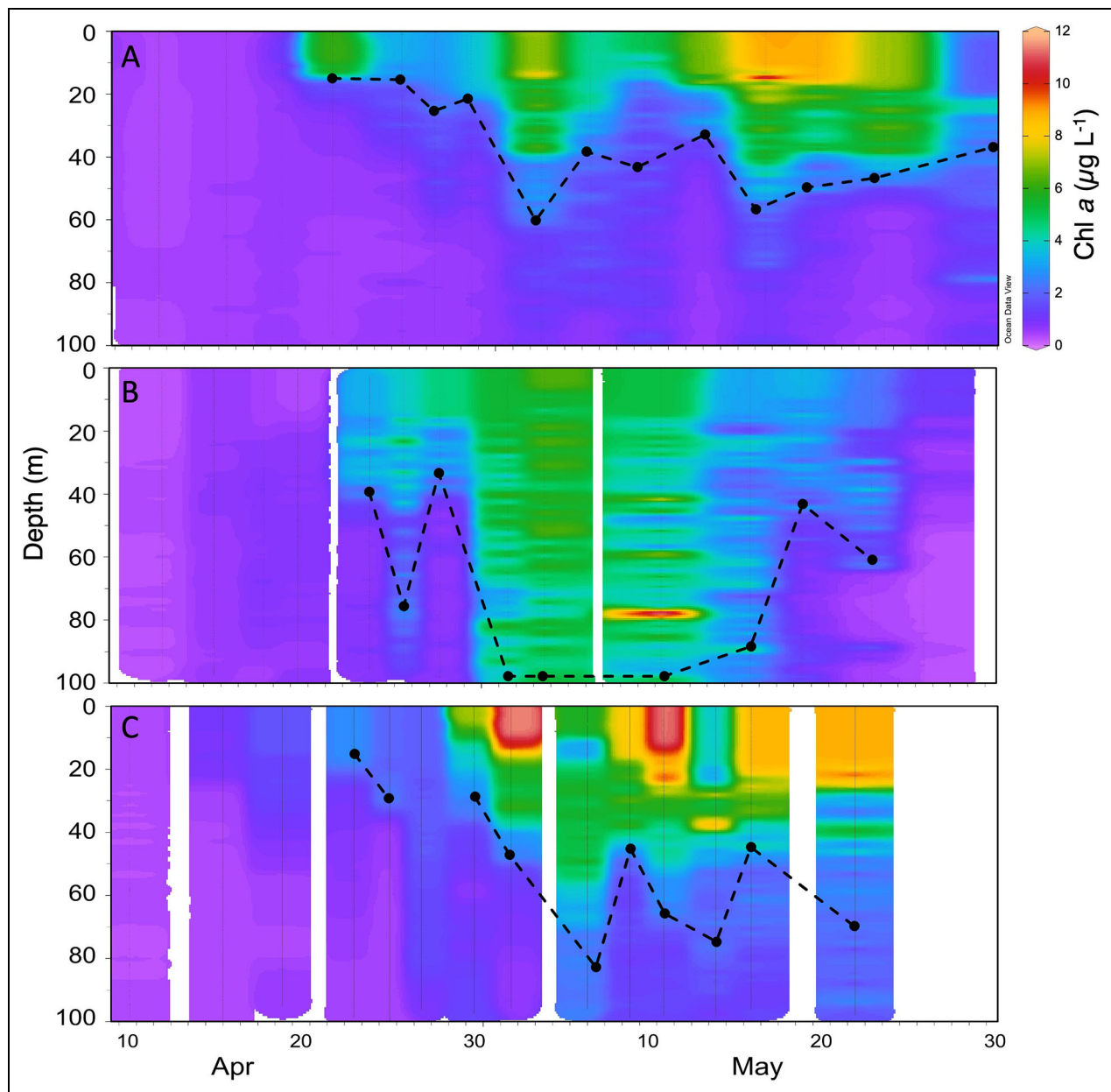


Figure 2. Time-depth resolved development of Chl *a* during the spring blooms in the three study years. Plots are based on corrected Chl *a* fluorescence measurements from CTD profiles during April and May of (A) 2016, (B) 2017, and (C) 2018. Black circles and dashed lines indicate the development of the estimated chlorophyll layer depth (CLD) based on a threshold level of $2.5 \mu\text{g Chl } a \text{ L}^{-1}$.

incoming PAR in the range of 370–695 nm was calculated by subtracting UV and IR, measured using pyranometers with different shading domes (Maturilli et al., 2019), from the global incoming radiation. Data were converted from planar measurements ($[\text{W m}^{-2}]$, 1π) to spherical data ($[\text{W m}^{-2}]$, 4π) as measured otherwise in this study. Data were further integrated to yield daily dose values.

Light attenuation with depth (attenuation coefficient, K_d) was estimated following the Beer–Lambert law (Pearson’s linear correlation, $r^2 > 0.94$ in all cases) over the entire data range per day, based on manually measured irradiance profiles using a cosine-corrected LI-192 underwater quantum sensor (LI-COR, Lincoln, NE, USA). At each measuring depth (0–25 m) data were recorded once measured values had stabilized (i.e., after 30–60 sec) and

corrected for changing incident irradiance based on simultaneous PAR measurements in air using a LI-190R quantum sensor (LI-COR, Lincoln, NE, USA) connected to the same datalogger. As PAR was measured directly below the sea surface (4–5 cm) as our first measurement step, surface specular reflectance is indirectly included in the fitted K_d . In cases of missing data, the K_d values of the closest two measurements were averaged. In 2018, no data were collected. K_d for depth-integrated net primary production (NPP) in 2018 was based on the average K_d values from both previous years measured in the respective week of each sampling date ($n = 10$), increasing the uncertainty of the 2018 NPP estimates but likely not introducing systematic errors, given that K_d did not differ significantly between the years (Table 2, Table S1).

Table 2. Environmental parameters (mean \pm standard deviation) during the spring bloom in April and May of 2016, 2017, and 2018

Year	Dataset	Temperature (°C)	n	Practical Salinity	n	Incident PAR ^a		K _d (m ⁻¹) ^b	n	Potential Density		CLD (m) ^d	n
						Dose (mol photons m ⁻² day ⁻¹)	n			Difference ^c	n		
2016	Full dataset	1.32 \pm 1.01	17	34.82 \pm 0.10	17	30.4 \pm 9.3	17	0.29 \pm 0.09	15	0.14 \pm 0.16	17	25 \pm 15	16
	Main bloom ^e	1.08 \pm 0.77	9	34.83 \pm 0.07	9	31.7 \pm 9.0	9	0.34 \pm 0.09	8	0.12 \pm 0.12	9	28 \pm 14	9
2017	Full dataset	2.33 \pm 0.48	15	35.04 \pm 0.04	15	31.7 \pm 6.6	15	0.31 \pm 0.10	9	0.03 \pm 0.05	15	61 \pm 32	14
	Main bloom	2.48 \pm 0.20	5	35.05 \pm 0.04	5	26.9 \pm 7.5	5	0.35 \pm 0.03	4	0.002 \pm 0.04	5	62 \pm 33	6
2018	Full dataset	-0.06 \pm 0.50	14	34.59 \pm 0.09	14	28.3 \pm 8.5	14	na ^f	na	0.16 \pm 0.13	14	27 \pm 10	14
	Main bloom	-0.13 \pm 0.28	7	34.60 \pm 0.06	7	28.3 \pm 2.2	7	na	na	0.13 \pm 0.07	7	33 \pm 10	6

^aPhotosynthetically active radiation.

^bLight attenuation coefficient with depth.

^cBetween 2 m and 95 m depths.

^dChlorophyll layer depth.

^eAt 10 m depth.

^fNot available.

2.4. Carbonate chemistry

Discrete samples from 10 m, 25 m, and 50 m water depth were collected by single 10 L Niskin hauls at station KB3. First, samples for the determination of dissolved inorganic carbon (DIC) and total alkalinity (TA) were collected directly from the Niskin bottles closely following Dickson et al. (2007). Samples were fixed with mercury chloride (final concentration 0.02%) and stored at 3–5°C in the dark until analysis on a VINDTA system (Versatile INstrument for the Determination of Total inorganic carbon and titration Alkalinity; Marianda, Kiel, Germany) following Dickson et al. (2007). The accuracy of the measurements (3 and 2 $\mu\text{mol kg}^{-1}$ for DIC and TA, respectively) was assured by daily analyses of Certified Reference Materials (CRM, provided by AG Dickson, Scripps Institution of Oceanography). Using TA, DIC, nutrients, and pressure for each sample, pCO_2 levels at 2°C were calculated using CO2SYS (Pierrot et al., 2006).

2.5. Nutrients

Nutrient samples from 10 m, 25 m, and 50 m depth were collected directly from the Niskin bottles. Duplicate samples per depth were filtered through 0.2 μm SFCA syringe filters (Nalgene, Thermo Fisher Scientific, Waltham, MA, USA). Syringes, filter, and polypropylene sampling tubes (Sarstedt, Nümbrecht, Germany) were rinsed with sample twice before samples were collected. In 2016 and 2017, samples were analyzed colorimetrically on a QuAatro autoanalyzer (Seal, WI, USA) within 12 h of sample collection. In 2018, nutrient samples were frozen directly at -20°C and analyzed on the same instrument in the home laboratory after thawing the samples for >18 h to allow full dissociation of silanole groups. Instrument performance was monitored by measuring certified reference materials (CRMs, JAMSTEC, Natsushimacho, Japan). Detection limits were 0.02 $\mu\text{mol L}^{-1}$ for NO_3^- , 0.004 $\mu\text{mol L}^{-1}$ for PO_4^{3-} , and 0.01 $\mu\text{mol L}^{-1}$ for Si(OH)_4 . Depth-integrated nutrient concentrations based on discrete measurements from the different depths were calculated via numerical integration.

2.6. Particulate organic matter

Particulate organic carbon (POC) and nitrogen (PN) were measured after gentle filtration onto precombusted (15 h, 500°C) GF/F filters (Whatman Maidstone, UK) and stored at -20°C . Samples were acidified with HCl to remove inorganic carbon and dried for at least 12 h at 60°C prior to sample preparation. Analysis was performed using a CHNS-O elemental analyser (Euro EA 3000, HEKAtech, Haaksbergen, Netherlands), using Acetanilide as a calibration standard. Concentrations of POC and PN were corrected for blank measurements and normalized to filtered volume.

2.7. Chlorophyll a

Water for Chl *a* samples was collected in 10 L carboys, which were stored cold and dark for 1–3 h until filtrations took place at the laboratory at $4 \pm 1^\circ\text{C}$. Samples were gently (maximum of 200 mBar) filtered onto precombusted GF/F filters (Whatman, Maidstone, UK) and immediately placed

into 6 mL 90% acetone. Samples were then homogenized using a cell mill (Precellys, Bertin Technologies SAS, Montigny-le-Bretonneux, France) and extracted at -20°C overnight. Chl *a* concentrations were measured on a fluorometer (Trilogy, Turner Designs, San Jose, USA), using an acidification step (0.01 M HCl final concentration) to determine phaeopigments (Knap et al., 1996).

2.8. Analysis of species composition by light microscopy

The presence and semi-quantitative relative abundances of marine protist groups and species were determined from handnet samples. During each sampling event, a small Apstein handnet (Hydro-Bios, Altenholz, Germany) with 20 μm mesh size was used to concentrate the protistan community via slow manual tows between 20 m and the surface. The concentrated sample was transferred into a 50 mL falcon tube, fixed with Lugols solution (1% final concentration) and stored in the dark at 4°C . At the home laboratory, samples were settled for 24–36 h in an Uthermoehl chamber (Hydro-Bios, Altenholz, Germany) and analyzed on an inverted light microscope (Axiovert Observer, Zeiss, Oberkochen, Germany). Five randomized overview images at $5\times$ magnification as well as 10–20 detailed pictures at larger magnification ($100\times$ to $200\times$) were taken from each sample. Based on the low magnification images, the present, dominant (approximately >15% of cell counts), and highly dominant (approximately >30% of cell counts) genera were determined; present genera were also identified on higher magnification images. Some of the dominant species (*Micromonas pusilla*, *Thalassiosira hyalina*, *T. gravida*, and *T. nordenskoeldii*) were identified by sequencing their internal transcribed spacer (ITS) rRNA regions and blasting them against database results (Wolf et al., 2017; Hoppe et al., 2018).

2.9. ^{14}C -based carbon fixation and net primary production

Potential carbon fixation of samples from 10 m and 25 m depths were determined in duplicate by incubation with 53.1 mCi mmol^{-1} $\text{NaH}^{14}\text{CO}_3$ (2.109 MBq mol^{-1} stock; Perkin Elmer, Waltham, USA) for 24 h under a fixed set of reference conditions ($1.5 \pm 0.6^\circ\text{C}$ and $30 \pm 6 \mu\text{mol photons m}^{-2} \text{s}^{-1}$ constant temperature and irradiance conditions). Irradiances correspond to daily average irradiance at 6–12 m water depth. Temperatures during the incubations differed slightly between years, with average values of $1.7 \pm 0.2^\circ\text{C}$ in 2016, $1.5 \pm 0.3^\circ\text{C}$ in 2017, and $1.3 \pm 0.4^\circ\text{C}$ in 2018 (Almemo 2890 temperature logger, Ahlborn, Holzkirchen, Germany). For each measurement, two 20 mL aliquots were incubated after addition of 10 $\mu\text{Ci NaH}^{14}\text{CO}_3$ (specific activity of 0.5 $\mu\text{Ci mL}^{-1}$). Details on the methods and potential differences between the three years can be found in the Supplementary materials (Text S2).

To investigate the light dependence of C fixation, photosynthesis-irradiance (PI) curves based on differing optical transmission of 50 mL incubation bottles (Hydro-Bios, Altenholz, Germany) were measured in samples from

10 m and 25 m depths. In 2016 and 2017, PI curves were conducted as 24 h in-situ incubations on a moored frame 0.5 m under the sea surface close to the harbor of Ny-Ålesund. In 2018, PI curve samples were incubated for 24 h under constant light in an ICES incubator (Hydro-Bios, Altenholz, Germany). PI curves of Chl *a*-specific 24 h carbon fixation were fitted as a function of irradiance (according to the formula by Webb et al., 1974). More details can be found in the Supplementary materials (Text S2).

For depth-integrated net primary production (NPP), the observed light-limited slope of the ^{14}C -based PI curves ($^{14}\text{C}_\alpha$) was used to calculate C fixation for the respective fluorescence-derived Chl *a* concentration and calculated irradiance for each depth (similarly as employed by Fernández-Méndez et al., 2015). Integrals of NPP over the upper 100 m were calculated via numerical integration.

2.10. Variable Chl *a* fluorescence

Photophysiological characteristics, based on photosystem II (PSII) variable Chl *a* fluorescence, were measured using a fast repetition rate fluorometric sensor (FRRf; FastOcean PTX, Chelsea Technologies, Molesey, UK) in combination with a FastAct Laboratory system (Chelsea Technologies, Molesey, UK). The excitation wavelength of the fluorometer's light-emitting diodes (LEDs) was 450 nm, and the applied excitation light intensity was $21,587 \mu\text{mol photons m}^{-2} \text{s}^{-1}$. The FRRf was used in single turnover mode, with a saturation phase comprising 100 flashlets on a 2 μs pitch and a relaxation phase comprising 40 flashlets on a 50 μs pitch. Measurements were conducted in a temperature-controlled chamber ($\pm 0.2^\circ\text{C}$) at the respective treatment temperature. After subtraction of a blank value, the minimum (F_0 and F_0' for light- and dark-acclimated measurements, respectively) and maximum Chl *a* fluorescence (F_m and F_m' for light- and dark-acclimated measurements, respectively) were estimated from iterative algorithms for induction (Kolber et al., 1998) and relaxation phase (Oxborough, 2012) after 15 min of dark acclimation, which was sufficient to achieve a dark-acclimated state (data not shown). All fluorescence parameters were calculated by standard equations (Genty et al., 1989; Maxwell and Johnson, 2000).

Fluorescence-based PI were conducted at six irradiances between 33 and $672 \mu\text{mol photons m}^{-2} \text{s}^{-1}$, with an acclimation time of 10 min per light step. Relative electron transfer rate through PSII ($\text{ETR} [\text{mol e}^- (\text{mol RCII})^{-1} \text{s}^{-1}]$) for each light step was calculated as detailed in Oxborough (2012). Following the suggestion by Silsbe and Kromkamp (2012), the light-limited slope, or light-use efficiency (ETR_α) and the maximum electron transfer rates per RCII (ETR_{max}) were estimated by fitting the data to the model by Webb et al. (1974). The photoacclimation parameter ETR_{E_k} was then calculated as $\text{ETR}_{\text{max}}/\text{ETR}_\alpha$.

2.11. Statistics

The non-parametric data used in this study were tested for normality via the Shapiro-Wilk test before conducting further statistical analyses. In four instances, data were not normally distributed and log transformation was performed (Table S1). To identify significant differences in

parameter values between years, ANOVAs with additional Tukey's pairwise posthoc tests were performed using the software Past4 (Hammer et al., 2001). As including pre- and post-bloom phases introduced considerable temporal variability and as the aim of this study was to compare the blooms of these years with each other rather than examining temporal changes, only data from the defined main bloom periods of the respective years were used for statistical analysis. All data are shown as averages with one standard deviation.

3. Results

We found that the main bloom period was always observable at 10 m in all years while not always at 25 m, making 10 m the most representative for bloom characteristics of our discrete sampling depths. This finding is congruent with CLDs always being deeper than 10 m, while CLDs exceeding 25 m occurred in only 60% of our observations. For our analysis, we therefore focus on the results from 10 m water depth and supplement them with mooring-based estimates and depth-integrated values. For completeness, we include data from 25 m in the figures. All discrete sampling data (from 10 m, 25 m, and 50 m sampling depths) are available at <https://doi.org/10.1594/PANGAEA.931854>.

3.1. Environmental conditions

The spring blooms occurred in the months of April and May in all three years. During this period, surface water temperatures generally increased. While all blooms started at water temperatures of $1.0\text{--}1.5^\circ\text{C}$ at 23–30 m depth on April 1, the rate of increase was highest in 2017 and lowest (with an intermittent decrease down to -0.5°C) in 2018 (Figure S2). Average temperatures at 10 m water depth were $1.08 \pm 0.77^\circ\text{C}$, $2.48 \pm 0.20^\circ\text{C}$, and $-0.13 \pm 0.28^\circ\text{C}$ in 2016, 2017, and 2018, respectively (Table 2). Surface salinity mirrored the differences between temperatures in the three years, with highest salinities in 2017 and lowest in 2018 (Figure 3, Tables 2 and S1).

At the latitude of our study site, the sun does not set below the horizon between April 17 and August 26. During the entire sampling period, daily average irradiances generally increased with the solar elevation (Figure 3C; Cohen et al., 2020) despite effects of cloud cover. Daily irradiance doses, that is, downwelling incident irradiance above the ocean surface, varied between 10.1 and $47.3 \text{ mol photons m}^{-2} \text{day}^{-1}$, with maximal hourly average values of 1000 to $1200 \mu\text{mol photons m}^{-2} \text{s}^{-1}$ on some days. Even though cloud cover led to variable irradiances on short time scales (Table 2), no significant differences between years were observed (Table S1). Light attenuation in the surface ocean was variable (K_d ranged from 0.14 to 0.47 m^{-1}), but tended to be highest in the beginning of May during the peak of the bloom. On average, K_d was similar in the 2 years it was measured, being $0.29 \pm 0.09 \text{ m}^{-1}$ in 2016 ($0.34 \pm 0.09 \text{ m}^{-1}$ during main bloom) and $0.31 \pm 0.10 \text{ m}^{-1}$ in 2017 ($0.35 \pm 0.03 \text{ m}^{-1}$ during main bloom; Tables 2 and S1).

Hourly averaged wind speeds varied between 1 m s^{-1} and 12 m s^{-1} , and did not differ significantly between

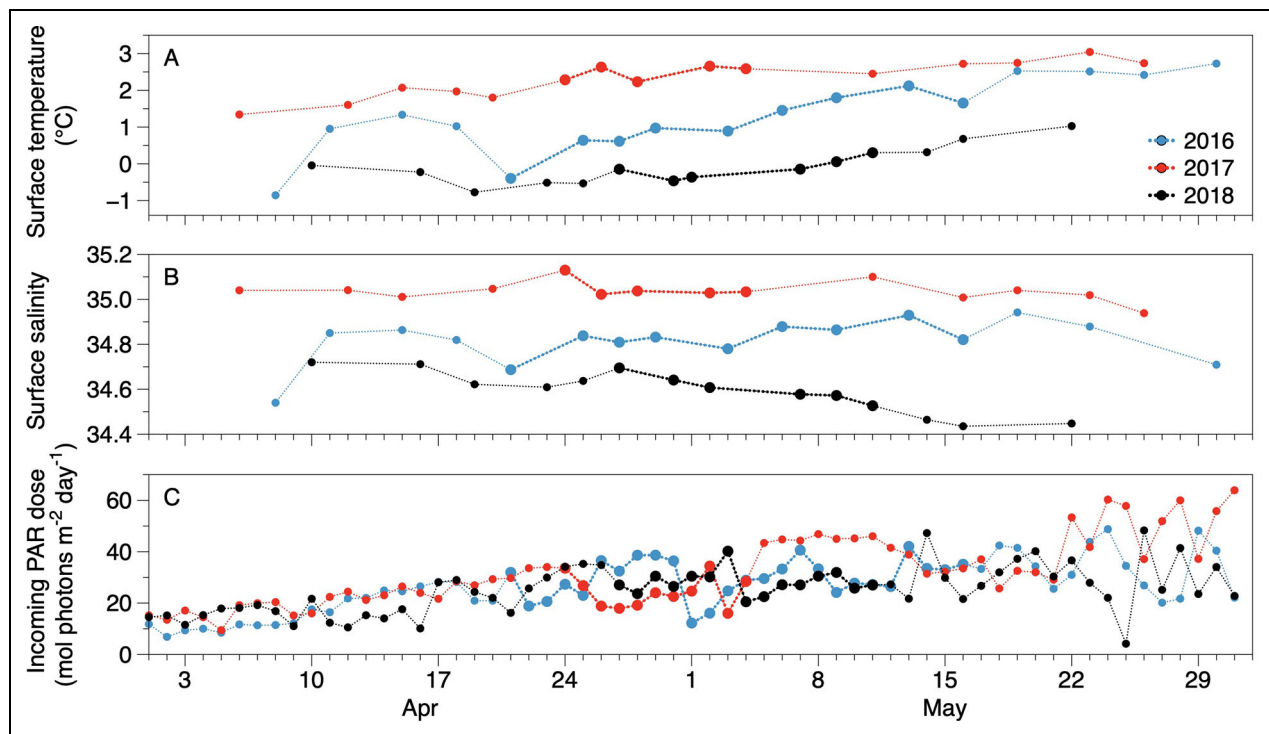


Figure 3. Environmental parameters during the spring bloom in the three study years. (A) Daily average temperature (°C); (B) salinity; and (C) incoming photosynthetically active radiation (PAR, mol photons m⁻² day⁻¹) during April and May 2016 (blue), 2017 (red), and 2018 (black). Thicker lines and larger symbols indicate the main bloom phases of all years.

years (Figure S3, **Tables 2** and S1). Wind directions were variable with the highest frequency in all years being from southeasterly directions, blowing from the glaciers, along the fjord axis (Table S1).

Profiles of water column properties (**Figures 2**, S3–S6) indicated that well-defined mixed layers were not present during the sampling campaign. Potential density profiles showed evidence of very weak layering over the main bloom phases of the study period (Figures S4–S6), indicative of a previously well-mixed water column (Figures S4–S6). Under these conditions, different classic definitions of the mixed layer depth resulted in highly variable MLD estimates that did not align with Chl *a* depth distribution (Figure S3). However, the difference in potential density between surface (2 m) and depth (95 m) during the main bloom phase (**Figure 4**) was larger in 2016 (0.15 ± 0.12) and 2018 (0.13 ± 0.07) compared to 2017 (0.002 ± 0.04).

The depth of the CLD varied within and between the different years (**Figure 4**, **Table 2**). The shallowest CLD of 15.5 m was observed in April 2016, while CLDs deeper than 100 m were observed in May 2017. The water column was characterized by rather shallow CLDs at the start of the sampling program in all years. CLDs during the main phase of the bloom, however, were significantly different between years (Table S1), with 2016 and 2018 exhibiting shallower CLDs (35 ± 17 m and 46 ± 23 m, respectively), and 2017 deeper and generally more variable CLDs (78 ± 29 m; Table S1). Maximum CLDs during this period were 61 m in 2016, >100 m in 2017, and 84 m in 2018.

3.2. Nutrients and other biogeochemically relevant properties

Surface nutrient concentrations at the beginning of April were similar in all years, with initial values of 11.2 ± 0.5 $\mu\text{mol L}^{-1}$ nitrate, 0.7 ± 0.1 $\mu\text{mol L}^{-1}$ phosphate, and 4.4 ± 0.2 $\mu\text{mol L}^{-1}$ silicate (**Figure 5**). Drawdown dynamics, however, were quite different between years. In 2016 and 2018, drawdown increased exponentially during the main biomass development of the bloom, but input pulses replenished nutrient levels several times in 2016, while surface nutrients quickly approached depletion in 2018 (**Figure 5**). In 2017, nutrient drawdown was slower than in the other years and lowered initial concentrations only by about half, as surface concentrations did not decrease below 5.9 ± 0.3 $\mu\text{mol L}^{-1}$ nitrate, 0.5 ± 0.01 $\mu\text{mol L}^{-1}$ phosphate, and 4.1 ± 0.3 $\mu\text{mol L}^{-1}$ silicate by the end of the bloom (**Figure 5**, **Table 3**). Nitrate-to-phosphate ratios were initially around 14–16 mol mol⁻¹ in all years (Table S1) and decreased slightly over the sampling period, without any clear differences between the three years (Figure S7). Similarly, initial nitrate-to-silicate ratios did not differ between years (Table S1), with values ranging between 2.5 and 3.5 (molar ratio; Figure S7). Reflecting the different dynamics in the individual nutrients, the latter ratios increased during the main bloom in 2016, decreased in 2017 and did not show any trend in 2018.

3.3. Bulk biomass development and stoichiometry

Surface Chl *a* concentrations in April and May of all years clearly illustrate the increase, peak, and decline of the

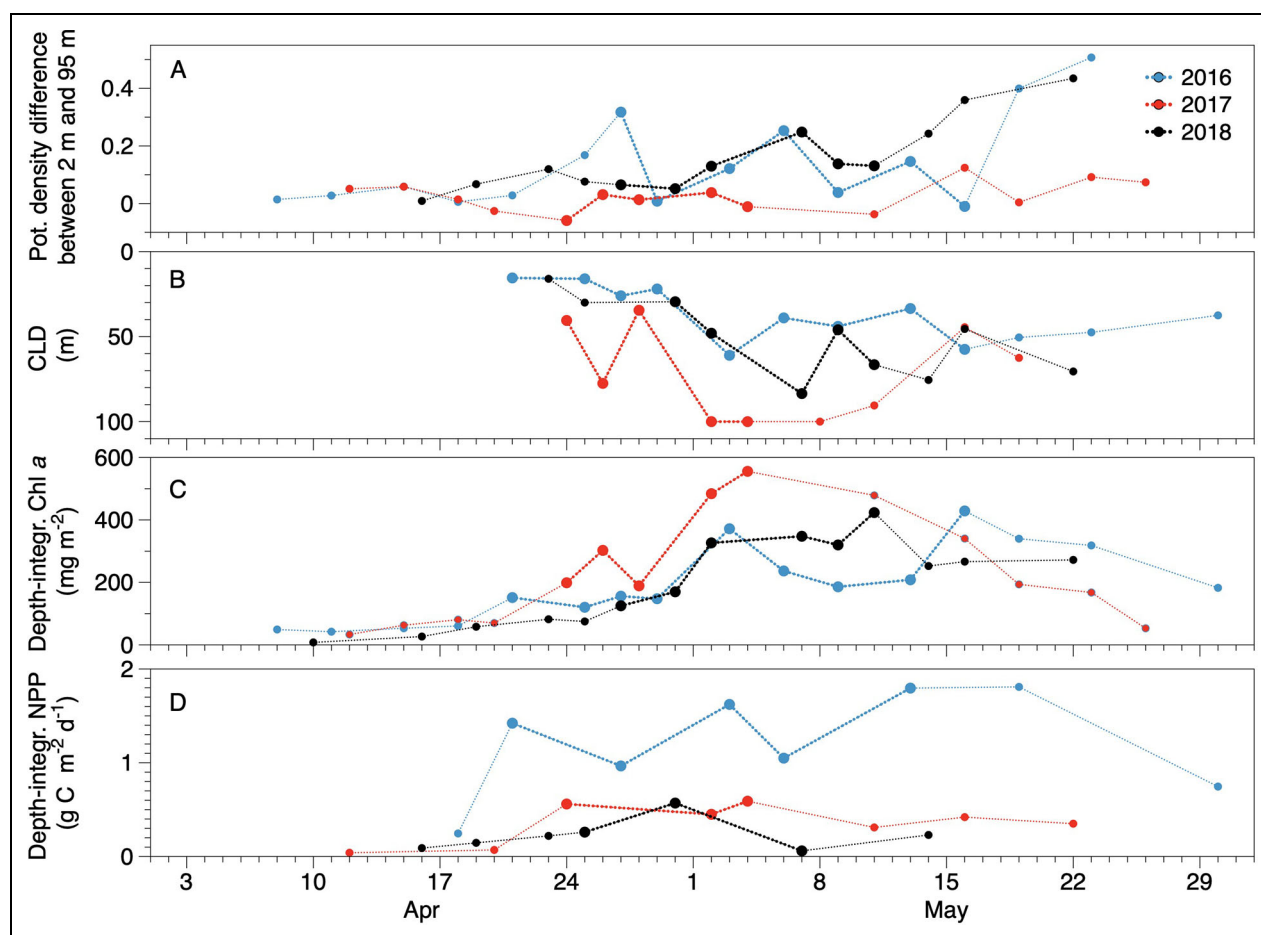


Figure 4. Stratification and general bloom development in the three study years. (A) Difference in potential density between depths of 2 m and 95 m; (B) chlorophyll layer depth (CLD, m); (C) depth-integrated Chl *a* inventories (mg m^{-2}); and (D) depth-integrated NPP ($\text{g C m}^{-2} \text{d}^{-1}$) in 2016 (blue), 2017 (red), and 2018 (black). Thicker lines and larger symbols indicate the main bloom phases of all years.

spring bloom (**Figure 6**). Initial values at 10 m were similar between years (0.11 , 0.18 , and $0.10 \mu\text{g L}^{-1}$ for 2016, 2017, and 2018, respectively). No significant differences were observed between years regarding either minimal or maximal values (Table S1). Highest Chl *a* concentrations at 10 m were reached on May 16, 2016 ($8.9 \mu\text{g L}^{-1}$), May 2, 2017 ($7.3 \mu\text{g L}^{-1}$), and May 11, 2018 ($7.14 \mu\text{g L}^{-1}$). Similarly, Chl *a* concentrations at 10 m depth decreased below $1 \mu\text{g L}^{-1}$ by the end of May in all years (**Figure 6**). Chl *a* values at 50 m were generally low, but increased up to $5.1 \mu\text{g L}^{-1}$ at different points in time in May, while surface values decreased at the same time (Figure S8). This indication for depth export of biomass was more pronounced in 2016 and 2018 compared to 2017. Generally, discrete Chl *a* concentrations measured at 10, 25, and 50 m depths over time reflected CLD dynamics, with more evenly distributed Chl *a* in deep CLDs (especially in 2017) and higher concentrations at 10 m and 25 m during bloom build-up in shallow CLDs (especially in 2016 and 2018; Figure S8).

Fluorescence-based depth-integrated Chl *a* standing stocks of the upper 100 m of the water column (**Figure 4**) indicate that the onset of the blooms, that is, the start of biomass accumulation, occurred before the start of the

sampling campaign in all years (i.e., before April 8, 2016, April 12, 2017, and April 10, 2018, respectively). The main bloom period occurred between mid-to-end of April and early-to-mid May in all years (**Table 1**). The timing of the bloom climax, with maximal rates of biomass accumulation, and of the apex, or peak, in biomass varied by a few days to weeks between years (**Figure 4**). In 2016, the climax occurred between May 13 and May 16, while the apex was observed on May 16. A slightly smaller climax and apex were already observed from April 29 to May 3. In 2017, both climax (April 28 to May 2) and apex (May 4) occurred earlier than in the year before. In 2018, the highest rate of biomass accumulation indicated the climax in the first week of May (April 30 to May 2), followed by an apex occurring on May 11. In terms of maximal absolute values, the highest integrated Chl *a* standing stocks were observed in 2017, followed by 2018 and 2016 (**Table 4**). While the integrated Chl *a* standing stocks over the main bloom phase were similar between years, the height of the apexes of the 2016 and 2017 blooms differed significantly (Table S1). In 2017, depth-integrated Chl *a* concentrations decreased more noticeably after the peak, while the decline was less pronounced in the other 2 years (**Figure 4**).

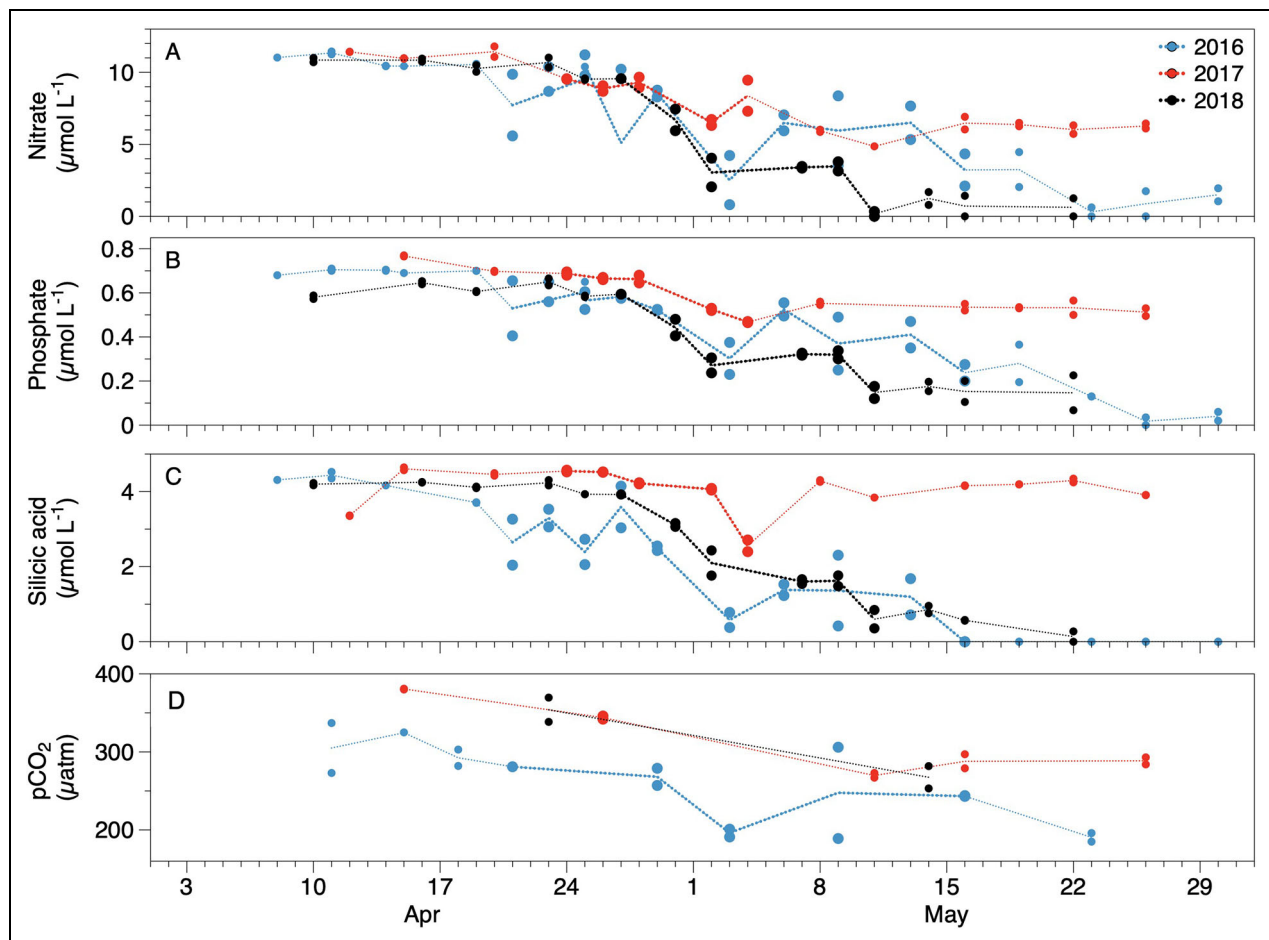


Figure 5. Near-surface nutrient concentrations and $p\text{CO}_2$ in the three study years. Concentrations ($\mu\text{mol L}^{-1}$) of (A) nitrate, (B) phosphate, and (C) silicic acid, and levels of (D) $p\text{CO}_2$ (μatm ; normalized to 2°C) from 10 m and 25 m depths (indicated by the same symbols to illustrate variability in surface ocean conditions) in 2016 (blue), 2017 (red), and 2018 (black). Thicker lines and larger symbols indicate the main bloom phases of all years.

Table 3. Dynamics of nutrients and $p\text{CO}_2$ (mean concentration \pm standard deviation) during the spring bloom in April and May of 2016, 2017, and 2018

Year	Bloom Timing ^a	Nitrate ($\mu\text{mol L}^{-1}$)	n	Silicic Acid ($\mu\text{mol L}^{-1}$)	n	Phosphate ($\mu\text{mol L}^{-1}$)	n	$p\text{CO}_2$ (μatm)	n
2016	Initial	11.14 ± 0.16	2	4.33 ± 0.03	2	0.69 ± 0.01	2	299 ± 37	2
	Final	0.98 ± 1.38	2	0.00 ± 0.00	2	0.03 ± 0.04	2	219 ± 33	2
2017	Initial	11.18 ± 0.35	2	4.00 ± 0.92	2	0.74 ± 0.05	2	364 ± 25	2
	Final	5.91 ± 0.27	2	4.13 ± 0.31	2	0.50 ± 0.01	2	281 ± 4	2
2018	Initial	10.72 ± 0.03	2	4.20 ± 0.05	2	0.61 ± 0.05	2	370	1
	Final	0.00 ± 0.00	2	0.28 ± 0.40	2	0.09 ± 0.03	2	253	1

^aInitial indicates first sampling event before main bloom development; final indicates last sampling event after the peak of the spring bloom.

Dynamics in carbon-to-Chl *a* ratios of the organic matter in the upper water column (C:Chl *a*) were characterized by highest values in the pre- and post-bloom situations (up to $1200 \text{ g C [g Chl } a]^{-1}$), and lowest values during climax and apex, despite high sample-to-sample variability (Figure 6). The 10 m C:Chl *a* ratios during the main phase of the bloom were 69 ± 12 , 54 ± 9 , and 71 ± 21 for 2016, 2017, and 2018, respectively (Table 4). Thus,

we considered C:Chl *a* ratios during the main bloom development to be rather constant within and between years (Table S1).

3.4. Taxonomic composition

The overall protist community in the upper 20 m of the water column observed in the three years was diverse, especially during the pre-climax phase of the bloom

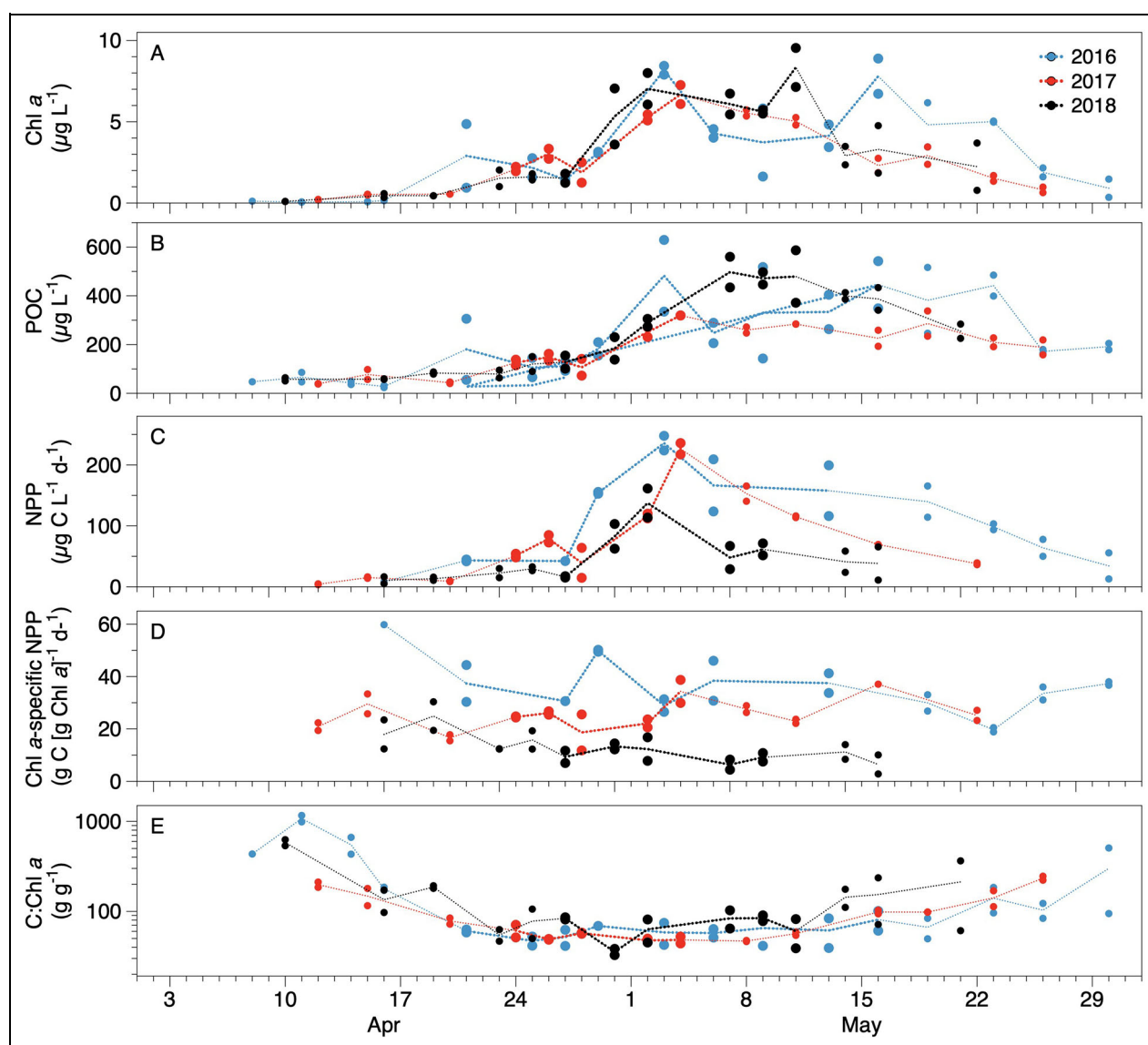


Figure 6. Near-surface photosynthetic biomass quantities and characteristics during the blooms in the three study years. Concentrations ($\mu\text{g L}^{-1}$) of (A) Chl *a* and (B) POC, rates of (C) potential net primary production (NPP, $\mu\text{g C L}^{-1} \text{d}^{-1}$) and (D) Chl *a*-specific potential carbon fixation ($\mu\text{g C [Chl } a]^{-1} \text{d}^{-1}$), and ratios of (E) C:Chl *a* (g g^{-1} ; note logarithmic scale) from 10 m and 25 m depths (indicated by the same symbols to illustrate variability in surface ocean conditions) depths in 2016 (blue), 2017 (red), and 2018 (black). Thicker lines and larger symbols indicate the main bloom phases of all years.

(Figure 7, Table S2). Cells in the upper 20 m of the water column represented different taxonomic and functional groups. Regarding diatoms, both pennate and centric genera were observed. Pennate diatoms consisted of *Navicula*, *Nitzschia*, and *Fragilariopsis* as the most dominant genera, but species belonging to the genera *Ceratoneis*/*Cylindrotheca*, *Pseudonitzschia*, and *Pleurosigma* were also present in many samples from all years. The group of centric diatoms was dominated by *Thalassiosira* and *Chaetoceros*, but *Bacteriosira*, *Odontella*, *Rhizosolenia*, and *Dactylisolen* also contributed to the assemblages. Further, picoplankton and flagellates (mainly single-celled and colonial *Phaeocystis* among others such as *Micromonas*), dinoflagellates (e.g., *Gymnodinium*, *Dinophysis*, *Prorocentrum*, *Prorocentrum*), silicoflagellates (mainly *Dictyocha*) and other

protistean grazers (mainly ciliates) contributed to the protist communities. In all years, the pre-climax assemblages were dominated by diatoms, while other groups contributed more to the post-bloom assemblages. Assemblage composition during the main phase of the bloom differed strongly between the three years.

In 2016, the main biomass development was dominated by centric diatoms from the *Thalassiosira* genus (cf. *T. hyalina*), especially during the climax and the first biomass peak in early May (Figure 7, Table S2). During the second and even higher biomass peak at mid-May, another smaller centric diatom, *Chaetoceros gelidus* (formerly and commonly referred to as *C. socialis*; Chamnansin et al., 2013) was even more abundant than *Thalassiosira*. The haptophyte *Phaeocystis pouchetii* contributed significantly to the protist biomass

Table 4. Measures of biomass and productivity (mean \pm standard deviation) during the spring bloom in April and May of 2016, 2017, and 2018

Year	Dataset	Chl <i>a</i>		Depth-integrated		POC ($\mu\text{mol L}^{-1}$)		POC:Chl <i>a</i>		Potential NPP ^a (g C L ⁻¹ d ⁻¹)		Chl <i>a</i> -specific NPP (g C [g Chl] ⁻¹ d ⁻¹)		Depth-integrated NPP (g C m ⁻² d ⁻¹)	
		($\mu\text{g L}^{-1}$)	n	Chl <i>a</i> (mg m ⁻²)	n	n	n	n	n	n	n	n	n	n	n
2016	Full dataset	3.4 \pm 2.9	17	188 \pm 121	16	23 \pm 17	17	226 \pm 304	17	129 \pm 79	10	34.4 \pm 9.9	10	1.2 \pm 0.6	8
	Main bloom	5.0 \pm 2.5	9	221 \pm 108	9	29 \pm 16	9	69 \pm 12	9	166 \pm 73	5	38.9 \pm 10.1	5	1.4 \pm 0.4	5
2017	Full dataset	2.9 \pm 2.2	14	228 \pm 177	14	16 \pm 8	14	98 \pm 62	14	79 \pm 68	11	24.1 \pm 3.7	11	0.4 \pm 0.2	8
	Main bloom	4.4 \pm 1.9	7	365 \pm 163	6	19 \pm 6	7	54 \pm 9	7	115 \pm 59	7	25.5 \pm 3.1	7	0.5 \pm 0.1	4
2018	Full dataset	3.1 \pm 2.6	14	242 \pm 148	14	22 \pm 16	14	158 \pm 163	14	39 \pm 36	11	10.7 \pm 6.2	11	0.2 \pm 0.2	7
	Main bloom	5.5 \pm 2.0	6	341 \pm 120	6	31 \pm 15	6	71 \pm 27	6	62 \pm 44	5	7.8 \pm 2.8	5	0.3 \pm 0.2	4

^a Net primary production.

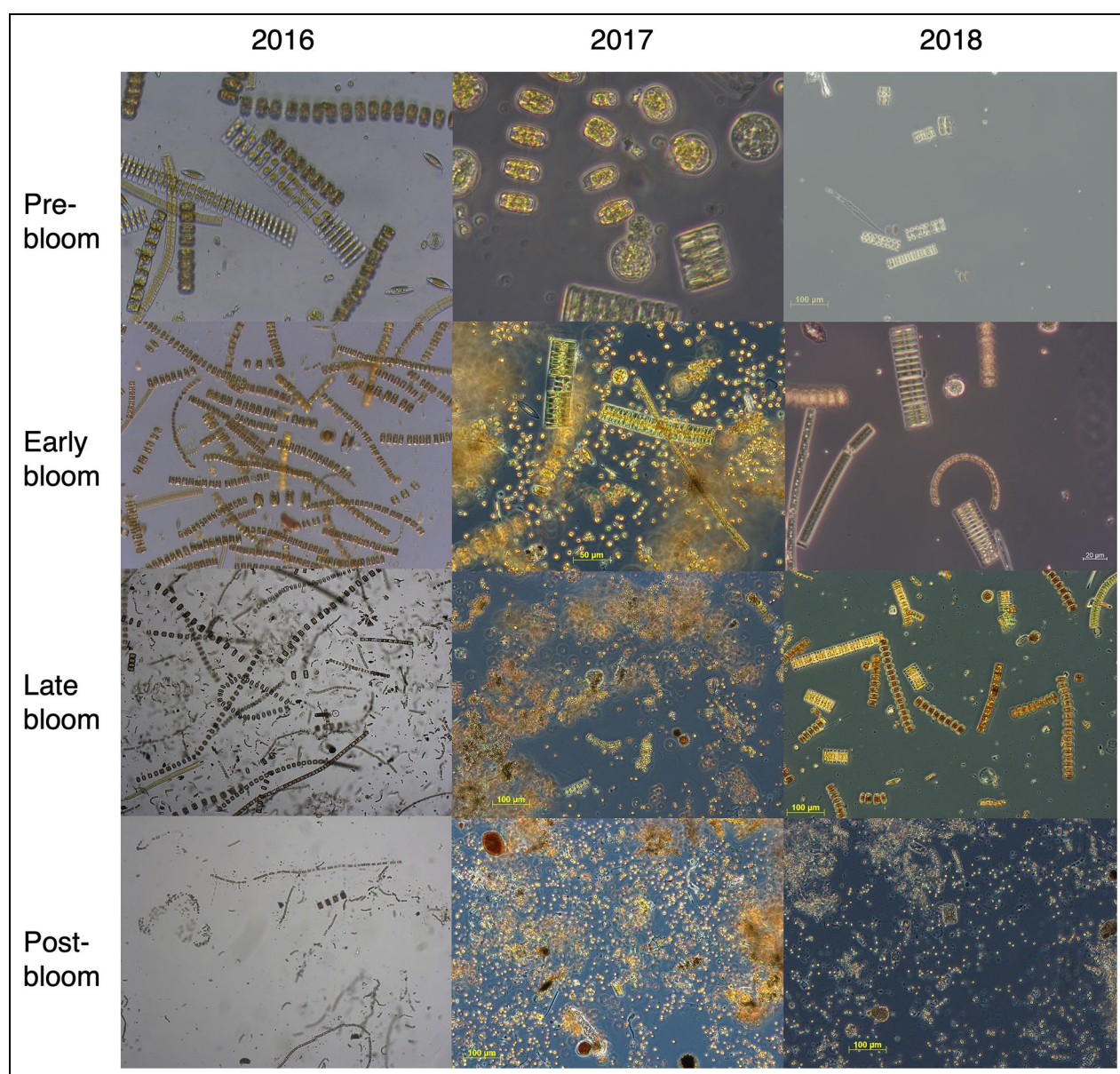


Figure 7. Species composition overview for the blooms in the three study years. Pre-bloom, early and late main bloom and post-bloom phase. As these samples were collected by hand net, they do not give a quantitative indication of overall biomass or abundances, only relative qualitative contributions.

from end of April onward, but did not dominate the assemblage (Table S2) in terms of numbers or biovolume. For the samples from the second half of May 2016, light microscopy revealed post-bloom conditions of fewer intact cells with strongly reduced Chl *a* content, many dinoflagellates, ciliates and other protistean grazers, as well as larger fecal pellets present in the net samples.

In 2017, the early pre-climax phase in mid-April was dominated by diatoms, with a mix of *Thalassiosira* and pennate diatom genera (*Navicula*, *Nitzschia*, and *Fragilariopsis*; **Figure 7**, Table S2). By April 24, that is, before the climax and well before the peak of the bloom, *Phaeocystis pouchetii* was dominating the protist assemblages in terms of numbers and biovolume, and remained the most abundant species well into the post-bloom conditions at the end of May. While in April there were many single *P. pouchetii* cells, colonies became more abundant and larger from the end

of April onward and were the most prominent feature in the climax and peak samples from mid-May.

In 2018, assemblages did not show a clear succession over time while remaining diverse, despite the formation of a large spring bloom (**Figure 7**, Table S2). Throughout the sampling period, pennate diatoms belonging to different species of the genera *Navicula*, *Nitzschia*, and *Fragilariopsis* dominated the assemblage. Centric *Thalassiosira* were present throughout the sampling period with a higher relative contribution in April, while *Chaetoceros* (mainly *C. gelidus*) occurred in higher abundances from May 9 onward, that is, during the second peak in biomass development and beyond. Single-celled and colonial *Phaeocystis pouchetii* increased in numbers throughout the month of May, but only dominated the protistean biomass during the declining phase of the bloom, that is, from mid-May to end of May and onward (Table S2).

3.5. Carbon fixation, net primary production, and photophysiology

We assessed Chl *a*-specific carbon fixation in samples from 10 m and 25 m depths under reference conditions ($1\text{--}2^\circ\text{C}$ and $30\ \mu\text{mol photons m}^{-2}\text{ s}^{-1}$) as an easily comparable measure of potential primary production of the phytoplankton assemblages in the three years (**Figure 6**). Chl *a*-specific potential carbon fixation from 10 m depth did not show any trends with bloom development, but was significantly higher in 2016 ($39 \pm 10\ \mu\text{g C} [\mu\text{g Chl } a]^{-1}\text{ d}^{-1}$) than in 2017 ($26 \pm 3\ \mu\text{g C} [\mu\text{g Chl } a]^{-1}\text{ d}^{-1}$) and in 2018, with the latter year showing the lowest rates ($8 \pm 3\ \mu\text{g C} [\mu\text{g Chl } a]^{-1}\text{ d}^{-1}$; **Tables 4** and S1).

In addition, light-dependence of Chl *a*-specific carbon fixation was measured. As PI curves did not saturate (**Figure S9**), only the light-limited slope $^{14}\text{C}_\alpha$ can be assessed. Based on (non-laboratory) in-situ incubations, $^{14}\text{C}_\alpha$ during the 2016 main bloom phase was significantly higher than in 2017 (**Tables 4** and S1). The laboratory-based assessment of $^{14}\text{C}_\alpha$ in 2018, which is not directly comparable to the in-situ data because of the constant versus naturally varying irradiances (Hoppe et al., 2015; White et al., 2020), resulted in much lower $^{14}\text{C}_\alpha$ values (**Table 5**).

Calculated depth-integrated NPP of the upper 100 m of the water column showed a similar pattern (**Figure 4**), with significantly higher average main bloom phase values in 2016 compared to 2017 (**Tables 4** and S1). In 2018, depth-integrated NPP was even lower (**Table 4**). These values depend on α , which was determined in the laboratory under constant light in 2018, and are not directly comparable to those determined in-situ under variable light in the two previous years.

FRRF-based photophysiological characteristics of the three blooms are described based on values from the main bloom phase at 10 m water depth (**Table 5**). Maximum quantum yields of PSII (F_v/F_m) were similar in 2016 (0.41 ± 0.06) and in 2018 (0.47 ± 0.05), but significantly lower in 2017 (0.32 ± 0.04 ; **Table S1**). The absorption cross section of PSII (ρ_{PSII}) was similar in all years (data not shown; see Hoppe et al., 2021). The connectivity between PSII reaction centers (ρ) differed between years, being lowest in 2017, followed by 2016, and highest in 2018 (**Table S1**). The re-opening rate of PSII reaction centers (τ) was similar in 2016 and 2018, but much higher in 2017 (**Table S1**).

FRRF-based PI curves revealed high variability but no significant differences between the photochemical light responses in ETR_α between 2016 and 2017 (**Table 5**; no FRRF-based PI curves were measured in 2018). Resulting FRRF_E_k values, however, were higher in 2016 than in 2017 (**Table S1**).

4. Discussion

4.1. Active mixing controls depth distribution of phytoplankton biomass

In biological oceanography, bloom development is often linked to the seasonally evolving stratification conditions in oceanic settings (Carvalho et al., 2017; Kara et al., 2000). However, the data from this study originate from a high-

latitude fjord (usually not ice-covered; Gerland et al., 2020). Such coastal environments typically experience a different cycle of seasonal stratification compared to oceanic settings (Cottier et al., 2010). Due to the lack of a pycnocline or strong stratification, neither classical temperature- or density-derived MLD definitions nor Brunt-Väisälä frequency maxima (as identified from CTD-derived density casts) seem adequate to investigate mixing-derived depth distribution of phytoplankton biomass (**Figure S3**). This conclusion fits well with observations that bio-optical properties and phytoplankton biomass are not evenly distributed within such mixed layers (Huisman et al., 1999; Franks, 2015; Carranza et al., 2018).

The system under examination, Kongsfjorden, is rather weakly stratified in spring (**Figures S4–S6**), and active mixing, primarily through wind effects, therefore exerts a strong control on the redistribution of primary producers (Carranza et al., 2018). Many studies on active mixing utilize turbulence profiling techniques to map the turbulent energy within the water column (e.g., Hopkins et al., 2021), which unfortunately were not available for this study. A larger difference between the potential density at 2 m and 95 m (**Table 2**) and a tendency toward increasing density differences over the main bloom periods (**Figure 4**) in 2016 and 2018 compared to 2017, however, still gives an indication of weaker mixing in the former two years.

Based on the observation of a non-homogeneously distributed Chl *a* layer (**Figure 2**), the biomass distribution in our dataset seems to be driven by a combination of current and past active mixing events as well as light-dependent biomass build-up in layers of past mixing activity (Carranza et al., 2018). While our operational definition of the CLD (bottom of the layer with $>2.5\ \mu\text{g Chl } a\text{ L}^{-1}$) simplified the complexity of the distinct depth distribution, it generally captured well the depth range with significant phytoplankton biomass and the differences between years (**Figure 2**). Some exceptions were found on specific sampling dates (e.g., end of April 2017 and mid-May 2018), when secondary biomass peaks at deeper locations in the water column, probably originating from sinking or past deeper mixing events, were picked up by the definition. As mixing in the fjord system regularly reaches depths of 100 m or more, cells below the mixing layer can regularly be reintroduced into it (**Figure 2**).

4.2. Bloom initiation was comparable between the three years

The three observed blooms were typical high-latitude spring blooms and fit the previously described spring bloom dynamics in Kongsfjorden in many ways (Hegseth et al., 2019). Consistent with the paradigm of nutrient replenishment during winter convection (Tremblay et al., 2015), nitrate concentrations measured in early April of each study year (approximately $11\ \mu\text{mol L}^{-1}$; **Table 3**) were close to the maximum values reported (Hegseth et al., 2019; Singh et al., 2020; van de Poll et al., 2020). Further, incoming irradiances were comparable (**Figure 3**), while winter and spring fast ice concentrations were similarly low in all those years, being restricted to the

Table 5. Photophysiological characteristics (mean \pm standard deviation) of phytoplankton during the spring bloom in April and May of 2016, 2017, and 2018

Photophysiological Parameters ^a												
Year	Dataset	F _V /F _m	n	ρ	n	τ (s ⁻¹)	n	ETR _{E_K} (μmol photons m ⁻² s ⁻¹)	n	ETR _α (mol e ⁻ [mol RCII] ⁻¹ [mol photons] ⁻¹)	¹⁴ C _α (g C [g Chl <i>a</i>] ⁻¹ d ⁻¹ [μmol quanta m ⁻² s ⁻¹] ⁻¹)	n
2016	Full dataset	0.39 ± 0.07	11	0.25 ± 0.09	11	696 ± 64	11	129 ± 16	8	0.69 ± 0.49	0.66 ± 0.14	8
	Main bloom	0.41 ± 0.06	8	0.26 ± 0.08	8	692 ± 54	8	126 ± 18	6	0.77 ± 0.54	0.69 ± 0.14	6
2017	Full dataset	0.33 ± 0.03	11	0.10 ± 0.06	6	966 ± 85	11	100 ± 31	11	0.86 ± 0.42	0.35 ± 0.15	11
	Main bloom	0.32 ± 0.04	6	0.06 ± 0.03	3	1006 ± 95	6	98 ± 36	6	0.91 ± 0.54	0.29 ± 0.09	6
2018	Full dataset	0.35 ± 0.19	6	0.28 ± 0.14	6	717 ± 146	6	na ^b	na	na	0.09 ± 0.02	na
	Main bloom	0.47 ± 0.05	3	0.36 ± 0.07	3	653 ± 41	3	na	na	na	0.09 ± 0.03	na

^aMaximum quantum yield of photosystem II (F_v/F_m), connectivity between PSII reaction centers (ρ), re-opening rate of PSII reaction centers (τ), ETR-based photoacclimation parameter (ETR_{E_K}), light-limited slope of electron transport per PSII reaction center (ETR _{α}), light-limited slope of C fixation per Chl *a* (¹⁴C _{α}).

^bNot available.

shallow areas of the inner fjord (Pavlova et al., 2019; Gerland et al., 2020). Thus, neither irradiances nor ice conditions drove the observed differences in bloom dynamics and composition at the sampled mid-fjord location (KB3; **Figure 1**). In all three years, initial Chl *a* concentrations ($0.07\text{--}0.19\ \mu\text{g L}^{-1}$) were already above reported Kongsfjorden winter values of $0.01\text{--}0.02\ \mu\text{g Chl } a\text{ L}^{-1}$ (Rokkan Iversen and Seuthe, 2011; Berge et al., 2015; Hoppe, 2022) but still low compared to the much higher values measured later in each year. Bloom initiation probably took place just before the start of our sampling program in all years, as depth-integrated biomass accumulation rates were still low but already positive (**Figure 4**) and nutrients were still maximal (**Figure 5**) as expected after winter mixing (Hegseth et al., 2019).

Especially in a highly advective system as Kongsfjorden (Tverberg et al., 2019), the blooms could have formed at a distance, not locally, and been advected into the fjord from Fram Strait. However, advective events often have the signature of rapid increases in temperature and/or salinity as new water masses enter the fjord (Willis et al., 2006). In our case, salinity remained relatively constant in all years while the Chl *a* fluorescence signal in the mooring data (Cottier et al., 2021a; Cottier et al., 2021b; Cottier et al., 2021c) increased continuously, which argues against major advection events during bloom formation (except for one event during the latter part of the 2016 bloom, discussed below). Furthermore, despite differences in water mass characteristics in the surface between years (colder and less saline water in April 2016 and 2018 than in April 2017; **Figure 3**, Table S1), pre-climax species composition was very similar in the three years (**Figure 7**, Table S2). According to Lampe et al. (2021), satellite-derived surface Chl *a* started to increase strongly in Atlantic waters off the Svalbard shelf in Fram Strait around mid-May in all years, thus long after the main phase of the bloom had started in Kongsfjorden. While advection of Atlantic water might have potentially influenced the later bloom development, the positive rates of C fixation, depth-integrated NPP rates and discrete Chl *a* data (**Figures 2, 4, and 6**), as well as lack of abrupt changes in species composition (Table S2), strongly support the idea that the observed blooms had formed locally. Similarly, while in early May 2016 the mooring data indicated mixing of local water masses with warmer and saltier water masses advected into the fjord (Figure S2), this mixing did not affect the gradual change in species composition, as both *Chaetoceros gelidus* and *Phaeocystis pouchetii* (which dominated the later bloom) started increasing their abundances before this advective event. Nitrate concentrations in this specific year, however, were already strongly depleted by the end of April, so that the replenishment of nutrients by an advective event allowed for a second peak with even higher biomass in May (**Figures 4 and 5**).

Our data on the build-up of the three observed blooms prior to and during the climax indicates that a shallowing of the upper mixing layer (caused by stable weather conditions) seems to allow for similar net biomass accumulation in all years but only once solar elevation has reached a certain threshold. While exponential biomass build-up in Kongsfjorden has been observed as early as February, it

was restricted to the upper few cm of the water column and disappeared as soon as turbulent mixing occurred (Hoppe, 2022). Independently of the degree of late winter mixing, blooms in Kongsfjorden have never been reported earlier than April (Hegseth et al., 2019; van de Poll et al., 2020), indicating that there is a low light threshold for bloom initiation as can be expected for high latitude systems such as Kongsfjorden.

4.3. CLD dynamics seem to control further biomass development and productivity

Focusing only on the main bloom phases of the three years (**Table 3**, **Figure 2**), we next assess similarities and differences in biomass accumulation of the three blooms. Despite the strong similarity in the temporal development of biomass between the three blooms (**Figures 2 and 4**), the highest integrated biomass inventories were observed on different days in the same time period, occurring between May 4 and May 16 of the three years. Somewhat counterintuitively, the timing of the three investigated apexes seemed to be positively correlated to the CLD, with the earliest peak occurring in the most deeply mixed year (i.e., 2017) and the latest peak occurring in the year with the shallowest CLD (i.e., 2016). In fact, the apex directly followed a deepening, not a shallowing, of the CLD in two of the three years (i.e., 2016 and 2017; **Figure 4**). Despite only covering three years, this observation is consistent with field data and modeling output from the Southern Ocean (Llort et al., 2015; Hoppe et al., 2017) and the Subarctic Atlantic (Paulsen et al., 2015; Paulsen et al., 2017; Graff and Behrenfeld, 2018), which show that large-scale blooms can develop in mixing layers >100 m and that biomass build-up and primary production can be positively correlated with CLD.

While a controlling role of light (and nutrients, which were not limiting during the spring bloom development in this study; **Table 3**) is most certainly relevant with regard to cell-specific growth rates or net carbon fixation of phytoplankton (compare increasing slopes of the PI curves measured in-situ and in the laboratory; Figure S9), another important factor that drives biomass accumulation rates needs to be considered: the variability in loss terms (Behrenfeld and Boss, 2018). While grazing rates were not measured in this study (and are generally often lacking in bloom studies for the Arctic), theoretical frameworks such as the *Disturbance Recovery Hypothesis* (Behrenfeld, 2010; Behrenfeld and Boss, 2018) may allow us to better understand potential underlying mechanisms of bloom dynamics in the current dataset. This hypothesis focuses on intermittent decoupling of gain and loss rates of phytoplankton due to physical disturbances (such as deepening of the mixing layer that reduces grazer-prey encounter rates), which can lead to increasing phytoplankton standing stocks (Behrenfeld and Boss, 2018).

While Chl *a* is commonly used as a proxy for phototrophic biomass due to easy sampling and well-established sensor-based approaches, Chl *a*-to-biomass ratios vary as a function of physiological status and species composition (Behrenfeld et al., 2008). Measurements of POC, on the other hand, consider all organic matter above $0.7\ \mu\text{m}$ in

size, thus also include heterotrophic components of the plankton. In the case of our study, C:Chl *a* ratios during the main bloom phase were in the lower range of those observed in Arctic phytoplankton under a large range of irradiance settings (Croteau et al., 2020), suggesting together with our light microscopic analyses (Table S2) that POC was composed primarily of phototrophic organisms during the main bloom phase. As C:Chl *a* ratios during this period were rather constant and did not differ between years (Figure 5, Table S1), depth-integrated Chl *a* standing stocks of the upper 100 m of the water column (Figure 4) serve as good indicators of overall biomass development during the blooms. By definition, both Chl *a* concentrations and depth-integrated standing stocks increase during bloom build-up. In our case they correlated only weakly with each other (Linear Pearson's r : $R^2 = 0.49$ and $p = 0.03$; Figure 8A), suggesting that increasing standing stocks are not caused simply by increasing biomass in the surface ocean that is then redistributed in the mixing layer. Furthermore, there was no correlation between depth-integrated Chl *a* and depth-integrated NPP (Linear Pearson's r : $R^2 = -0.44$ and $p = 0.27$; Figure 8B), suggesting that biomass standing stocks were not controlled primarily by biomass production rates. Instead, we find the strongest correlation, by far, between 100 m depth-integrated standing stocks and CLD (Linear Pearson's r : $R^2 = 0.87$ and $p = 0.01$; Figure 8C). Given that nutrients were non-limiting and did not affect biomass build-up (Figure S10) and that the non-saturating PI curves measured in-situ (Figure S9) indicate that primary production should have been increasingly light-limited with increasing CLD, the positive relationship of depth-integrated standing stocks with CLD strongly argues against bottom-up controls. Based on the lack of evidence for bottom-up controlled dynamics in the three years studied, we therefore conclude that loss terms have a stronger influence on overall bloom dynamics than gains.

Further indications for the impact of loss terms on bloom dynamics stem from the fact that both Chl *a* concentrations and integrated biomass accumulation were higher in 2018 compared to 2016, even though the potential for primary production (i.e., Chl *a*-specific carbon fixation under reference conditions) was significantly lower in 2018 (Figures 4 and 6, Table 4). While temperatures during the 2018 incubations were lower, they represent well the range of in-situ temperature (Table 2) and should provide a good estimate of primary productivity (under irradiances typical for shallow CLDs) in that year. The differences in potential for primary production between 2016 and 2018 suggests that differences in loss rates such as grazing led to the similarly high biomass build-up in the two years. The warmer temperatures in 2016 compared to 2018 could have contributed to that similarity despite lower production in 2018, as grazer metabolism and feeding respond more strongly to increasing temperature than does primary production (Rose and Caron, 2007; Vaquer-Sunyer et al., 2010; Alcaraz et al., 2014). Furthermore, the main bloom period in 2016 consisted of a higher proportion of more lightly silicified diatoms

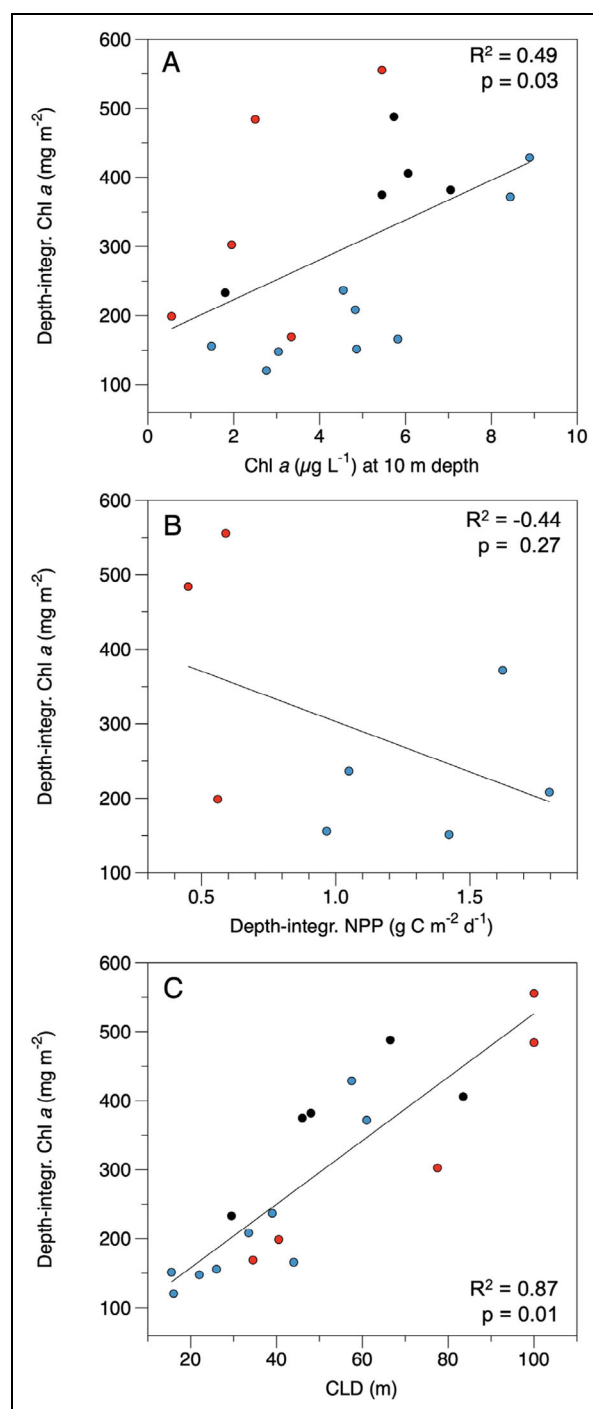


Figure 8. Relationships between primary production, biomass and chlorophyll layer depth in the three study years. Pearson's r linear correlations (black lines) of depth-integrated Chl *a* (mg m^{-2}) with (A) Chl *a* concentrations at 10 m depth, (B) depth-integrated net primary production (NPP, $\text{g C m}^{-2} \text{d}^{-1}$), and (C) chlorophyll layer depth (CLD, m) during the main bloom phases of 2016 (blue), 2017 (red), and 2018 (black). NPP from 2018 (Table 4) is not included in (B) as it was measured by a different method and thus is not directly comparable.

(belonging to the genera of *Thalassiosira* and *Chaetoceros*) that are a better food source for grazers, while more heavily silicified diatoms dominated the main bloom

period in 2018 (e.g., belonging to the genera of *Nitzschia*, *Navicula*, and *Fragilariopsis*) that are better protected against grazing (Liu et al., 2016; Zhang et al., 2017; Pančić et al., 2019). The usual time lag between phytoplankton and mesozooplankton grazers (Dalpadado et al., 2020) could have affected particularly the later part of the main bloom phase, and thus maximal standing stocks and bloom duration rather than composition.

Despite uncertainty in the fine-tuning of underlying mechanisms, our dataset from an Arctic coastal system provides some evidence that increased CLDs due to, for example, mixing layer deepening can have a positive effect on primary productivity. We hypothesize that changes in overall phytoplankton biomass development in highly dynamic Arctic systems can be controlled by disturbances such as mixing layer deepening, which lead to a decoupling of growth and grazing rates of phytoplankton. This concept as proposed in the framework of the *Disturbance Recovery Hypothesis* (Behrenfeld, 2010; Behrenfeld and Boss, 2018), to our knowledge has only been shown in the Arctic using satellite data, not discrete measurements (Behrenfeld et al., 2017). While our dataset does not fully test the *Disturbance Recovery Hypothesis*, it does add evidence of the relevance of some of its aspects, namely the dilution of phytoplankton biomass via deeper CLDs and the potential for that dilution to alleviate grazing pressure.

4.4. CLD also correlates with taxonomic composition

Despite differences in CLD, the most striking difference between the three blooms was their species composition. We observed diatoms to dominate the 2016 and 2018 blooms that were characterized by shallow depth distribution, while *Phaeocystis* dominated the deep CLD of the 2017 bloom (Figure 7, Table S2). Also, an increasing proportion of *Phaeocystis* was generally associated with a deepening of CLD in all years, while the shallow preclimax situation was always dominated by diatoms (e.g., beginning of May 2016, mid-April 2017, end of April 2018; Figures 2 and 7, Table S2).

Our physiological measurements aimed at acquiring a process-based understanding of the underlying mechanisms that allow different species and/or functional groups to be successful. Our data indicate that diatoms are indeed better competitors under shallow CLDs: diatom-dominated blooms in 2016 and 2018 exhibited a higher quantum yield efficiency (F_v/F_m ; Table 5) and a tendency toward higher values of the photoacclimation parameter ETR_{E_K} than the *Phaeocystis*-dominated assemblages in 2018. Also, a higher connectivity between reaction centers (ρ) and a shorter RCII reopening rate (τ) in the diatom-dominated assemblages supports previous findings that this group is better equipped for dealing with high-light stress (Lavaud, 2007; Trimborn et al., 2014; Kvernvik et al., 2020) and overall make more effective use of high-light peaks of the dynamic light fields in the fjords (Hoppe et al., 2015; Croteau et al., 2020; Kvernvik et al., 2021). These photophysiological characteristics acquired during the main bloom phase not only differed between years

(especially 2016 vs. 2017), but also between diatom- and *Phaeocystis*-dominated phases of the 2016 and 2018 blooms (Figure 7, Table S2).

While our photophysiological data can explain well why diatoms benefit from shallow CLD (under nutrient replete conditions as observed during the bloom climax), we are lacking evidence for *Phaeocystis* being better adapted for deeply mixed, even more strongly light-limited conditions. The light-limited slope of electron transport ($FRRF_{\alpha}$; Table 5) did not differ between years, but the light-limited slope of carbon fixation ($^{14}C_{\alpha}$) was much lower in the *Phaeocystis*-dominated compared to the diatom-dominated year, also causing the energy transfer efficiency from photochemistry to carbon fixation to be lower in the former. Thus, although previously postulated that Arctic *Phaeocystis* is particularly adapted to low light (Rokkan Iversen and Seuthe, 2011; Assmy et al., 2017), our data indicate that light is not the main factor controlling species dominance in Kongsfjorden, despite the strong correlation with CLD. Also, diatom-dominated blooms can be observed in mixing layers as deep as 100 m (Smetacek et al., 2012; Hoppe et al., 2017), suggesting that this group does not have a general disadvantage under deep mixing.

Other common explanations for the dominance of *Phaeocystis* versus diatoms include nutrient ratios, deep convection, and the advection of warmer and more saline water masses from subarctic regions. Ardyna et al. (2020) suggested for under-ice phytoplankton blooms that *Phaeocystis* dominates when $NO_3^-:Si(OH)_4$ ratios are >1 . For Kongsfjorden, this explanation does not hold, as initial $NO_3^-:Si(OH)_4$ ratios were >1 and $Si(OH)_4$ concentrations above $4 \mu mol L^{-1}$ were observed in all years, independently of whether diatoms or *Phaeocystis* dominated the bloom (Table 3; van de Poll et al., 2020). Also, in contrast to previous suggestions (Hegseth and Tverberg, 2013; Hegseth et al., 2019; Assmy et al., 2023), differences in seeding from surface sediment does not seem to be the driver of diatom versus *Phaeocystis* dominance in our dataset, as deep convection reaching the diatom seed bank in the sediment in late winter and early spring (Hegseth et al., 2019) was observed in all three years (Figure S11), with strongest depth-to-surface coupling in temperature and salinity actually occurring in the *Phaeocystis*-dominated year 2017.

As physiological characteristics and primary production rates of the blooms do not suggest bottom-up driven advantages of *Phaeocystis* during bloom formation, top-down mechanisms (e.g., grazing, virus infections) again likely play an important role here. Following the principles behind the *Disturbance Recovery Hypothesis* and acknowledging the understudied role of top-down control for Arctic bloom development, we hypothesize that grazing pressure may be key in driving the dominance of *Phaeocystis* versus diatoms during the spring bloom. Similar to chain formation of many bloom-forming diatoms, colony formation represents an escape by size-type behavior, with large *P. pouchetii* colonies being outside the prey spectrum of most grazers in the Arctic (Nejstgaard et al., 2007). Microzooplankton grazing, which is a very

important component of grazing pressure on phytoplankton (Landry and Calbet, 2004), will still have a much stronger impact on single-celled *Phaeocystis* than on colonies or diatoms. A deepening of the CLD during bloom build-up with lowered grazer-prey encounter probability thus may reduce grazing pressure more strongly for small single-celled *Phaeocystis* than for either chain-forming (2016) or strongly silicified (2018) diatoms, as larger zooplankton such as large copepods are also known to move actively toward their prey and could therefore be expected to be less affected by prey dilution (Folt and Burns, 1999; Smetacek, 2001; Friedrichs et al., 2013).

Phaeocystis has been shown to overwinter during the polar night in single cell stage in surface waters (Vader et al., 2015), and its colonies usually grow from single cells at the beginning of a bloom (Rousseau et al., 1994; Wassmann et al., 2005; Nejstgaard et al., 2007). Because the single-celled stage as well as the initial small colonies are most vulnerable to grazing, reduced grazer encounter rates under deepening CLDs before the bloom apex can have a huge effect on bloom composition, as this time of lowered grazing may allow *Phaeocystis* to grow colonies large enough to escape grazers due to their size (Ryderheim et al., 2022). In 2017, a strong deepening of the CLD was observed exactly during this period (**Figure 2**) and coincided with increasing colony formation (Table S1), while the two diatom-dominated spring blooms were characterized by consistently shallow CLDs during the initial and the apex phases (**Figures 2, 4, and 7**). To which degree this pattern can be generalized has yet to be evaluated. In any case, our hypothesis that their depth distribution regulates the dominance of diatoms versus *Phaeocystis* is in line with observations from other areas of the Arctic (Reigstad et al., 2002; Degerlund and Eilertsen, 2009). Also in Kongsfjorden, previous studies have reported diatom blooms in shallow waters and the dominance of *Phaeocystis* in deeply distributed spring blooms (Hegseth and Tverberg, 2013; Van de Poll et al., 2016; Assmy et al., 2023). Despite potentially strong differences in photophysiological adaptation, for example, with respect to trace metal availability, our observations also agree with some from the Southern Ocean, where *Phaeocystis antarctica* has been observed to dominate regularly over diatoms in deeper mixed layers (Goffart et al., 2000; Arrigo et al., 2010; Smith et al., 2013).

Understanding the drivers of species composition of spring blooms matters, because *Phaeocystis*-dominated blooms in the Arctic are often characterized by weaker carbon export to depth compared to diatom-dominated ones (e.g., Reigstad and Wassmann, 2007; Wiedmann et al., 2020). In accordance with such previous findings, we show that in a fjord system the drawdown of inorganic carbon for surface waters and the subsequent potential or increased CO₂ uptake from the atmosphere was also larger in the diatom-dominated 2016 bloom compared to the *Phaeocystis*-dominated bloom in 2017 (**Figure 5, Table 3**). The low carbon flux in the *Phaeocystis*- compared to the diatom-dominated bloom supports our hypothesis that its large colonies could not be efficiently grazed upon by mesozooplankton (Ryderheim et al., 2022), which in turn

would produce efficiently sinking fecal pellets (Henson et al., 2019), and that viral lysis could be a more plausible reason for bloom termination in 2019. These results not only highlight the importance of understanding the drivers of species dominance in the natural system, but also illustrate that inferring consequences for carbon drawdown from changes in bulk carbon fixation rates, without considering further ecological and physiological characteristics, can be misleading.

5. Conclusions

There is a long-standing debate on whether light, nutrients or both are the most important drivers of Arctic primary production (Arrigo et al., 2008; Tremblay et al., 2015). Based on our specific dataset, we propose to put more focus on additional, well recognized but largely understudied control mechanisms of Arctic bloom dynamics: top-down drivers such as grazing pressure or viral lysis, mediated by active mixing and changes in phytoplankton depth distribution. Although our study does not contain data on the grazer community, the comprehensive measurements of bottom-up related parameters argue against any other controlling factors. While the end of polar night sets a clear boundary with regard to the alleviation of light limitation and the timing of spring bloom initiation in Kongsfjorden, biomass dynamics *during* the bloom appear to correlate positively instead of negatively with CLD (**Figure 8**).

In the past years, the role of increased mixing and subsequent entrainment of new nutrients into surface waters (due to more open water and stronger winds) for high Arctic pelagic primary production has gained increasing attention (Ardyna et al., 2014; Crawford et al., 2020). While our fjord-focused data from spring are not directly transferable to this phenomenon, they nonetheless highlight the need to also test the extent to which decreased grazing rates contribute to the positive correlation between wind speed and primary production, especially as these other studies focused mainly on satellite data and did not provide (in-situ) nutrient measurements. For coastal systems such as Kongsfjorden in the future, warming and concurrent increasing local stratification may counteract the loss of ice-associated stratification, leading to diatom-dominated shallower mixing layers with high productivity but lower biomass build-up. Based on the surprising lack of evidence for bottom-up controls in our dataset, we suggest that changes in wind patterns and water column stability (e.g., advection, warming, meltwater and riverine inputs) in concert with poorly understood grazing pressure and viral dynamics may be as important drivers of change as the commonly discussed light and nutrient effects. Predicting future Arctic spring bloom phenology and productivity requires understanding the effects of disturbances (such as active mixing driven dynamics) on both gain and loss rates of phytoplankton.

Data accessibility statement

Biological and biogeochemical datasets for this research are available on Pangaea under <https://doi.org/10.1594/PANGAEA.931854> (Hoppe et al., 2021) and <https://doi.pangaea.de/10.1594/PANGAEA.944856> (Hoppe et al.,

2022). Oceanographic mooring data are available under <https://doi.org/10.11582/2021.00061> (Cottier et al., 2021a), <https://doi.org/10.11582/2021.00062> (Cottier et al., 2021b), and <https://doi.org/10.11582/2021.00065> (Cottier et al., 2021c). Meteorological data are available under <https://doi.pangaea.de/10.1594/PANGAEA.914979> (Maturilli et al., 2020a) and <https://doi.org/10.1594/PANGAEA.914927> (Maturilli et al., 2020b).

Supplemental files

The supplemental files for this article can be found as follows:

Text S1. Evaluation of classical estimates for mixed layer depth and their relevance for Kongsfjorden phytoplankton depth distribution.

Text S2. Methods details for ^{14}C -based carbon fixation.

Figure S1. Development of different estimates for mixed layer depth and Chl a distribution for the three years.

Figure S2. Mooring-based daily average temperature and salinity for the three years.

Figure S3. Wind speeds and direction compared to CLD and photosynthetic biomass for the three years.

Figure S4. CTD-based potential density profiles from 2016.

Figure S5. CTD-based potential density profiles from 2017.

Figure S6. CTD-based potential density profiles from 2018.

Figure S7. Development of surface macronutrient ratios in the three years.

Figure S8. Depth-resolved Chl a concentrations in the three years.

Figure S9. Photosynthesis-Irradiance relationships for the blooms in the three years.

Figure S10. Relationships of primary production and standing stocks with nitrate concentrations in the three years.

Figure S11. Temporal development of salinity at the surface and bottom from mooring deployments.

Table S1. Results from ANOVAS with normality and posthoc tests.

Table S2. Presence table of different protist groups and taxa.

Acknowledgments and funding

This work would not have been possible without the support by the AWIPEV station teams of 2016–2018 as well as L. Heitmann's help with fieldwork. T. Brenneis, L. Heitmann, and M. Machnik are acknowledged for support during laboratory analyses, D. Vogedes for help with the moorings, and J. Wloka for help with data analysis. This work received further funding by the Research Council of Norway, as part of the FAABulous project (Future Arctic Algae Blooms—and their role in the context of climate change, grant no. 243702). The mooring work was supported by NFR projects Marine Night (#226471) and FAABulous (#243702). KW's participation in field work was partially covered by Arctic Field Grants, awarded by Svalbard Science Forum. Additional support for FC's

contribution came from the Arctic PRIZE (PRoductivity in the seasonal Ice Zone) project (grant no. NE/P006302/1) funded by the UK Natural Environment Research Council (NERC) Changing Arctic Ocean program. We acknowledge support by the Open Access publication fund of Alfred-Wegener-Institut Helmholtz-Zentrum für Polar- und Meeresforschung.

Competing interests

There are no competing interests to declare.

Author contributions

Contributed to conception and design: CJMH, EL, BR.

Contributed to acquisition of data: CJMH, KKEW, FC, MM.

Contributed to analysis and interpretation of data: CJMH, KKEW, FC, EL, MM, BR.

Drafted and/or revised the article: CJMH, KKEW, FC, EL, MM, BR.

Approved the submitted version for publication: CJMH, KKEW, FC, EL, MM, BR.

References

- Alcaraz, M, Felipe, J, Grote, U, Arashkevich, E, Nikishina, A. 2014. Life in a warming ocean: Thermal thresholds and metabolic balance of arctic zooplankton. *Journal of Plankton Research* **36**: 3–10. DOI: <https://doi.org/10.1093/plankt/fbt111>.
- Ardyna, M, Arrigo, KR. 2020. Phytoplankton dynamics in a changing Arctic Ocean. *Nature Climate Change* **10**: 892–903. DOI: <https://doi.org/10.1038/s41558-020-0905-y>.
- Ardyna, M, Babin, M, Devred, E, Forest, A, Gosselin, M, Raimbault, P, Tremblay, J-É. 2017. Shelf-basin gradients shape ecological phytoplankton niches and community composition in the coastal Arctic Ocean (Beaufort Sea). *Limnology and Oceanography* **62**: 2113–2132. DOI: <https://doi.org/10.1002/lno.10554>.
- Ardyna, M, Babin, M, Gosselin, M, Devred, E, Rainville, L, Tremblay, J-É. 2014. Recent Arctic Ocean sea ice loss triggers novel fall phytoplankton blooms. *Geophysical Research Letters* **41**: 6207–6212. DOI: <https://doi.org/10.1002/2014GL061047>.
- Ardyna, M, Mundy, CJ, Mills, MM, Oziel, L, Grondin, P-L, Lacour, L, Verin, G, van Dijken, G, Ras, J, Alou-Font, E, Babin, M, Gosselin, M, Tremblay, J-É, Raimbault, P, Assmy, P, Nicolaus, M, Claustre, H, Arrigo, KR. 2020. Environmental drivers of under-ice phytoplankton bloom dynamics in the Arctic Ocean. *Elementa: Science of the Anthropocene* **8**. DOI: <https://doi.org/10.1525/elementa.430>.
- Arrigo, KR, Mills, MM, Kropuenske, LR, van Dijken, GL, Alderkamp, AC, Robinson, DH. 2010. Photophysiology in two major Southern Ocean phytoplankton taxa: Photosynthesis and growth of *Phaeocystis antarctica* and *Fragilariopsis cylindrus* under different irradiance levels. *Integrative and Comparable Biology* **50**: 950–966. DOI: <https://doi.org/10.1093/icb/icq021>.

- Arrigo, KR, van Dijken, G, Pabi, S. 2008. Impact of a shrinking Arctic ice cover on marine primary production. *Geophysical Research Letters* **35**: L19603. DOI: <https://doi.org/10.1029/2008gl035028>.
- Assmy, P, Fernández-Méndez, M, Duarte, P, Meyer, A, Randelhoff, A, Mundy, CJ, Olsen, LM, Kauko, HM, Bailey, A, Chierici, M, Cohen, L, Doulgeris, AP, Ehn, JK, Fransson, A, Gerland, S, Hop, H, Hudson, SR, Hughes, N, Itkin, P, Johnsen, G, King, JA, Koch, BP, Koenig, Z, Kwasniewski, S, Laney, SR, Nicolaus, M, Pavlov, AK, Polashenski, CM, Provost, C, Rösel, A, Sandbu, M, Spreen, G, Smedsrud, LH, Sundfjord, A, Taskjelle, T, Tatarek, A, Wiktor, J, Wagner, PM, Wold, A, Steen, H, Gran-skog, MA. 2017. Leads in Arctic pack ice enable early phytoplankton blooms below snow-covered sea ice. *Scientific Reports* **7**: 40850. DOI: <https://doi.org/10.1038/srep40850>.
- Assmy, P, Kvernvik, AC, Hop, H, Hoppe, CJM, Chierici, M, David, TD, Duarte, P, Fransson, A, García, LM, Patuła, W, Kwaśniewski, S, Maturilli, M, Pavlova, O, Tatarek, A, Wiktor, JM, Wold, A, Wolf, KKE, Bailey, A. 2023. Seasonal plankton dynamics in Kongsfjorden during two years of contrasting environmental conditions. *Progress in Oceanography* **213**: 102996. DOI: <https://doi.org/10.1016/j.pocean.2023.102996>.
- Assmy, P, Smetacek, V. 2009. Algal blooms, in Schaechter, M ed., *Encyclopedia of microbiology*. Oxford, UK: Elsevier: 27–41.
- Behrenfeld, MJ. 2010. Abandoning Sverdrup's Critical Depth Hypothesis on phytoplankton blooms. *Ecology* **91**: 977–989. DOI: <https://doi.org/10.1890/09-1207.1>.
- Behrenfeld, MJ, Boss, ES. 2018. Student's tutorial on bloom hypotheses in the context of phytoplankton annual cycles. *Global Change Biology* **24**: 55–77. DOI: <https://doi.org/10.1111/gcb.13858>.
- Behrenfeld, MJ, Halsey, KH, Milligan, AJ. 2008. Evolved physiological responses of phytoplankton to their integrated growth environment. *Philosophical Transactions of the Royal Society B: Biological Sciences* **363**(1504): 2687–2703. DOI: <https://doi.org/10.1098/rstb.2008.0019>.
- Behrenfeld, MJ, Hu, Y, O'Malley, RT, Boss, ES, Hostetler, CA, Siegel, DA, Sarmiento, JL, Schulien, J, Hair, JW, Lu, X, Rodier, S, Scarino, AJ. 2017. Annual boom–bust cycles of polar phytoplankton biomass revealed by space-based lidar. *Nature Geoscience* **10**(2): 118–122. DOI: <https://doi.org/10.1038/ngeo2861>.
- Berge, J, Daase, M, Renaud, PE, Ambrose, WG Jr, Darnis, G, Last, KS, Leu, E, Cohen, JH, Johnsen, G, Moline, MA, Cottier, F, Varpe, Ø, Shunatova, N, Bałazy, P, Morata, N, Massabuau, J-C, Falk-Petersen, S, Kosobokova, K, Hoppe, CJM, Węśławski, JM, Kukliński, P, Legeżyńska, J, Nikishina, D, Cusa, M, Kędra, M, Włodarska-Kowalczyk, M, Vogedes, D, Camus, L, Tran, D, Michaud, E, Gabrielsen, TM, Granovitch, A, Gonchar, A, Krapp, R, Callesen, TA. 2015. Unexpected levels of biological activity during the polar night offer new perspectives on a warming Arctic. *Current Biology* **25**: 2555–2561. DOI: <https://doi.org/10.1016/j.cub.2015.08.024>.
- Bischof, K, Convey, P, Duarte, P, Gattuso, J-P, Granberg, M, Hop, H, Hoppe, C, Jiménez, C, Lisitsyn, L, Martinez, B, Roleda, MY, Thor, P, Wiktor, JM, Gabrielsen, GW. 2019. Kongsfjorden as harbinger of the future Arctic: Knowns, unknowns and research priorities, in Hop, H, Wiencke, C eds., *The ecosystem of Kongsfjorden, Svalbard*. Cham, Switzerland: Springer: 537–562. (Advances in polar ecology; vol. 2). DOI: https://doi.org/10.1007/978-3-319-46425-1_14.
- Brainerd, KE, Gregg, MC. 1995. Surface mixed and mixing layer depths. *Deep Sea Research Part I: Oceanographic Research Papers* **42**(9): 1521–1543. DOI: [https://doi.org/10.1016/0967-0637\(95\)00068-H](https://doi.org/10.1016/0967-0637(95)00068-H).
- Carmack, E, Wassmann, P. 2006. Food webs and physical–biological coupling on pan-Arctic shelves: Unifying concepts and comprehensive perspectives. *Progress in Oceanography* **71**: 446–477. DOI: <https://doi.org/10.1016/j.pocean.2006.10.004>.
- Carranza, MM, Gille, ST, Franks, PJS, Johnson, KS, Pinkel, R, Garton, JB. 2018. When mixed layers are not mixed. Storm-driven mixing and bio-optical vertical gradients in mixed layers of the Southern Ocean. *Journal of Geophysical Research: Oceans* **123**(10): 7264–7289. DOI: <https://doi.org/10.1029/2018JC014416>.
- Carvalho, F, Kohut, J, Oliver, MJ, Schofield, O. 2017. Defining the ecologically relevant mixed-layer depth for Antarctica's coastal seas. *Geophysical Research Letters* **44**: 338–345. DOI: <https://doi.org/10.1002/2016GL071205>.
- Chamnansinp, A, Li, Y, Lundholm, N, Moestrup, Ø. 2013. Global diversity of two widespread, colony-forming diatoms of the marine plankton, *Chaetoceros socialis* (syn. *C. radians*) and *Chaetoceros gelidus* sp. nov. *Journal of Phycology* **49**: 1128–1141. DOI: <https://doi.org/10.1111/jpy.12121>.
- Cohen, JH, Berge, J, Moline, MA, Johnsen, G, Zolich, AP. 2020. Light in the polar night, in Berge, J, Johnsen, G, Cohen, JH eds., *Polar night marine ecology*. Cham, Switzerland: Springer: 37–66. (Advances in polar ecology; vol. 4). DOI: https://doi.org/10.1007/978-3-030-33208-2_3.
- Constable, AJ, Harper, S, Dawson, J, Holsman, K, Mustonen, T, Piepenburg, D, Rost, B. 2022. Polar regions. Climate Change 2022: Impacts, Adaptation, and Vulnerability. WG II to the 6th Assessment Report of the Intergovernmental Panel on Climate Change (IPCC). Cambridge, UK; New York, NY: Cambridge University Press.
- Cornec, M, Claustre, H, Mignot, A, Guidi, L, Lacour, L, Poteau, A, D'Ortenzio, F, Gentili, B, Schmechtig, C. 2021. Deep chlorophyll maxima in the global ocean: Occurrences, drivers and characteristics. *Global*

- Biogeochemical Cycles* **35**(4): e2020GB006759. DOI: <https://doi.org/10.1029/2020GB006759>.
- Cottier, F, Berge, J, Dumont, E, Griffith, C, Beaton, J, Vogedes, DL.** 2021a. Temperature, salinity, light and fluorescence (CTD) measurements from the Kongsfjorden (Svalbard) marine observatory (mooring) August 2016–August 2017. NIRD. DOI: <https://doi.org/10.11582/2021.00062>.
- Cottier, F, Berge, J, Griffith, C, Dumont, E, Beaton, J, Vogedes, DL.** 2021b. Temperature, salinity, light and fluorescence (CTD) measurements from the Kongsfjorden (Svalbard) marine observatory (mooring) September 2015–August 2016. NIRD. DOI: <https://doi.org/10.11582/2021.00061>.
- Cottier, F, Berge, J, Vogedes, D, Dumont, E, Beaton, J, Griffith, C, Kopec, T.** 2021c. Temperature, salinity, light and fluorescence (CTD) measurements from the Kongsfjorden (Svalbard) marine observatory (mooring) August 2017–August 2018. NIRD. DOI: <https://doi.org/10.11582/2021.00065>.
- Cottier, F, Skogseth, R, David, D, Berge, J.** 2019. Temperature time-series in Svalbard fjords. A contribution from the “Integrated Marine Observatory Partnership (iMOP).” SESS report 2018: The State of Environmental Science in Svalbard—An annual report. Longyearbyen: Svalbard Integrated Arctic Earth Observing System (SIOS).
- Cottier, FR, Nilsen, F, Skogseth, R, Tverberg, V, Skarøhamar, J, Svendsen, H.** 2010. Arctic fjords: A review of the oceanographic environment and dominant physical processes. *Geological Society, London, Special Publications* **344**: 35. DOI: <https://doi.org/10.1144/SP344.4>.
- Crawford, AD, Krumhardt, KM, Lovenduski, NS, van Dijken, GL, Arrigo, KR.** 2020. Summer high-wind events and phytoplankton productivity in the Arctic Ocean. *Journal of Geophysical Research: Oceans* **125**: e2020JC016565. DOI: <https://doi.org/10.1029/2020JC016565>.
- Croteau, D, Guérin, S, Bruyant, F, Ferland, J, Campbell, DA, Babin, M, Lavaud, J.** 2020. Contrasting nonphotochemical quenching patterns under high light and darkness aligns with light niche occupancy in Arctic diatoms. *Limnology and Oceanography* **66**: S231–S245. DOI: <https://doi.org/10.1002/lno.11587>.
- Dalpadado, P, Arrigo, KR, van Dijken, GL, Skjoldal, HR, Bagøien, E, Dolgov, AV, Prokopchuk, IP, Sperfeld, E.** 2020. Climate effects on temporal and spatial dynamics of phytoplankton and zooplankton in the Barents Sea. *Progress in Oceanography* **185**: 102320. DOI: <https://doi.org/10.1016/j.pocean.2020.102320>.
- Degerlund, M, Eilertsen, HC.** 2009. Main species characteristics of phytoplankton spring blooms in NE Atlantic and Arctic waters (68–80°N). *Estuaries and Coasts* **33**: 242–269. DOI: <https://doi.org/10.1007/s12237-009-9167-7>.
- Dickson, AG, Sabine, CL, Christian, JR.** 2007. *Guide to best practices for ocean CO₂ measurements*. Sidney, Canada: North Pacific Marine Science Organization.
- Falkowski, PG, Barber, RT, Smetacek, V.** 1998. Biogeochemical controls and feedbacks on ocean primary production. *Science* **281**: 200–206. DOI: <https://doi.org/10.1126/science.281.5374.200>.
- Fernández-Méndez, M, Katlein, C, Rabe, B, Nicolaus, M, Peeken, I, Bakker, K, Flores, H, Boetius, A.** 2015. Photosynthetic production in the central Arctic Ocean during the record sea-ice minimum in 2012. *Biogeosciences* **12**(11): 3525–3549. DOI: <https://doi.org/10.5194/bg-12-3525-2015>.
- Folt, CL, Burns, CW.** 1999. Biological drivers of zooplankton patchiness. *Trends in Ecology & Evolution* **14**: 300–305. DOI: [https://doi.org/10.1016/S0169-5347\(99\)01616-X](https://doi.org/10.1016/S0169-5347(99)01616-X).
- Franks, PJS.** 2015. Has Sverdrup's critical depth hypothesis been tested? Mixed layers vs. turbulent layers. *ICES Journal of Marine Science* **72**: 1897–1907. DOI: <https://doi.org/10.1093/icesjms/fsu175>.
- Friedrichs, L, Hörnig, M, Schulze, L, Bertram, A, Jansen, S, Hamm, C.** 2013. Size and biomechanic properties of diatom frustules influence food uptake by copepods. *Marine Ecology Progress Series* **481**: 41–51.
- Genty, B, Briantais, JM, Baker, NR.** 1989. The relationship between the quantum yield of photosynthetic electron transport and quenching of chlorophyll fluorescence. *Biochimica Biophysica Acta* **990**: 87–92. DOI: [https://doi.org/10.1016/s0304-4165\(89\)80016-9](https://doi.org/10.1016/s0304-4165(89)80016-9).
- Gerland, S, Pavlova, O, Divine, D, Negrel, J, Dahlke, S, Johansson, AM, Maturilli, M, Semmling, M.** 2020. Long-term monitoring of landfast sea ice extent and thickness in Kongsfjorden, and related applications (FastIce), in Van den Heuvel, F, Hübner, C, Błaszczuk, M, Heimann, M, Lihavainen, H eds., SESS Report 2019. Longyearbyen: Svalbard Integrated Arctic Earth Observing System: 160–167.
- Goffart, A, Catalano, G, Hecq, JH.** 2000. Factors controlling the distribution of diatoms and *Phaeocystis* in the Ross Sea. *Journal of Marine Systems* **27**: 161–175. DOI: [https://doi.org/10.1016/S0924-7963\(00\)00065-8](https://doi.org/10.1016/S0924-7963(00)00065-8).
- Graff, JR, Behrenfeld, MJ.** 2018. Photoacclimation responses in subarctic Atlantic phytoplankton following a natural mixing-restratification event. *Frontiers in Marine Science* **5**. DOI: <https://doi.org/10.3389/fmars.2018.00209>.
- Hamm, C, Reigstad, M, Wexels Riser, C, Mühlebach, A, Wassmann, P.** 2001. On the trophic fate of *Phaeocystis pouchetii*. VII. Sterols and fatty acids reveal sedimentation of *P. pouchetii*-derived organic matter via krill fecal strings. *Marine Ecology Progress Series* **209**: 55–69.
- Hamm, CE, Rousseau, V.** 2003. Composition, assimilation and degradation of *Phaeocystis globosa*-derived fatty acids in the North Sea. *Journal of Sea Research* **50**: 271–283. DOI: [https://doi.org/10.1016/S1385-1101\(03\)00044-3](https://doi.org/10.1016/S1385-1101(03)00044-3).
- Hammer, Ø, Harper, DAT, Ryan, PD.** 2001. PAST: Paleontological statistics software package for education and data analysis. *Palaeontologia Electronica* **4**: 9.

- Hasle, GR, Heimdal, BR.** 1998. The net phytoplankton in Kongsfjorden, Svalbard, July 1988, with general remarks on species composition of Arctic phytoplankton. *Polar Research* **17**(1): 31–52. DOI: <https://doi.org/10.3402/polar.v17i1.6605>.
- Hegseth, EN, Assmy, P, Wiktor, J, Kristiansen, S, Leu, E, Tverberg, V, Gabrielsen, GW, Skogseth, R, Cottier, FR.** 2019. Phytoplankton seasonal dynamics in Kongsfjorden, Svalbard and the adjacent shelf, in Hop, H, Wiencke, C eds., *The ecosystem of Kongsfjorden, Svalbard*. Cham, Switzerland: Springer: 173–227. (Advances in polar ecology; vol. 2).
- Hegseth, EN, Tverberg, V.** 2013. Effect of Atlantic water inflow on timing of the phytoplankton spring bloom in a high Arctic fjord (Kongsfjorden, Svalbard). *Journal of Marine Systems* **113–114**: 94–105. DOI: <http://dx.doi.org/10.1016/j.jmarsys.2013.01.003>.
- Henson, S, Le Moigne, F, Giering, S.** 2019. Drivers of carbon export efficiency in the global ocean. *Global Biogeochemical Cycles* **33**(7): 891–903. DOI: <http://dx.doi.org/10.1029/2018GB006158>.
- Hodal, H, Falk-Petersen, S, Hop, H, Kristiansen, S, Reigstad, M.** 2012. Spring bloom dynamics in Kongsfjorden, Svalbard: Nutrients, phytoplankton, protozoans and primary production. *Polar Biology* **35**: 191–203. DOI: <https://doi.org/10.1007/s00300-011-1053-7>.
- Hop, H, Cottier, F, Berge, J.** 2019. Autonomous marine observatories in Kongsfjorden, Svalbard, in Hop, H, Wiencke, C eds., *The ecosystem of Kongsfjorden, Svalbard*. Cham, Switzerland: Springer: 515–533. (Advances in polar ecology; vol. 2). DOI: https://doi.org/10.1007/978-3-319-46425-1_13.
- Hopkins, JE, Palmer, MR, Poulton, AJ, Hickman, AE, Sharples, J.** 2021. Control of a phytoplankton bloom by wind-driven vertical mixing and light availability. *Limnology and Oceanography* **66**: 1926–1949. DOI: <https://doi.org/10.1002/lno.11734>.
- Hoppe, CJM.** 2022. Always ready? Primary production of Arctic phytoplankton at the end of the polar night. *Limnology & Oceanography Letters* **7**(2): 167–174. DOI: <https://doi.org/10.1002/lol2.10222>.
- Hoppe, CJM, Flintrop, CM, Rost, B.** 2018. The Arctic picoeukaryote *Micromonas pusilla* benefits synergistically from warming and ocean acidification. *Biogeosciences* **15**: 4353–4365. DOI: <https://doi.org/10.5194/bg-2018-28>.
- Hoppe, CJM, Holtz, L-M, Trimborn, S, Rost, B.** 2015. Ocean acidification decreases the light-use efficiency in an Antarctic diatom under dynamic but not constant light. *New Phytologist* **207**: 159–171. DOI: <https://doi.org/10.1111/nph.13334>.
- Hoppe, CJM, Klaas, C, Ossebaar, S, Soppa, MA, Cheah, W, Laglera, LM, Santos-Echeandia, J, Rost, B, Wolf-Gladrow, DA, Bracher, A, Hoppema, M, Strass, V, Trimborn, S.** 2017. Controls of primary production in two phytoplankton blooms in the Antarctic Circumpolar Current. *Deep Sea Research* Part II: Topical Studies in Oceanography **138**: 63–73. DOI: <https://doi.org/10.1016/j.dsr2.2015.10.005>.
- Hoppe, CJM, Wischniewski, L, Wolf, KKE, Cottier, F, Rost, B.** 2021. Biogeochemical and ecophysiological monitoring at station KB3 in Kongsfjorden (2014–2018). PANGAEA. DOI: <https://doi.org/10.1594/PANGAEA.931854>.
- Hoppe, CJM, Wischniewski, L, Wolf, KKE, Cottier, F, Rost, B.** 2022. Depth integrated biogeochemical and ecophysiological monitoring at station KB3 in Kongsfjorden (2016–2018), Version 2. PANGAEA. DOI: <https://doi.org/10.1594/PANGAEA.944856>.
- Hsiao, SIC.** 1980. Quantitative composition, distribution, community structure and standing stock of sea ice microalgae in the Canadian Arctic. *Arctic* **33**: 768–793.
- Huisman, J, van Oostveen, P, Weissing, FJ.** 1999. Critical depth and critical turbulence: Two different mechanisms for the development of phytoplankton blooms. *Limnology and Oceanography* **44**(7): 1781–1787. DOI: <https://doi.org/10.4319/lo.1999.44.7.1781>.
- Inall, ME, Nilsen, F, Cottier, FR, Daae, R.** 2015. Shelf/fjord exchange driven by coastal-trapped waves in the Arctic. *Journal of Geophysical Research: Oceans* **120**: 8283–8303. DOI: <https://doi.org/10.1002/2015JC011277>.
- Jassby, AD, Platt, T.** 1976. Mathematical formulation of the relationship between photosynthesis and light for phytoplankton. *Limnology and Oceanography* **21**: 540–547.
- Kara, AB, Rochford, PA, Hurlburt, HE.** 2000. An optimal definition for ocean mixed layer depth. *Journal of Geophysical Research: Oceans* **105**: 16803–16821. DOI: <https://doi.org/10.1029/2000JC900072>.
- Knap, A, Michaels, A, Close, A, Ducklow, H, Dickson, A** eds. 1996. Protocols for the Joint Global Ocean Flux Study (JGOFS) Core Measurements. JGOFS Report No. 19. UNESCO.
- Kolber, ZS, Prasil, O, Falkowski, PG.** 1998. Measurements of variable chlorophyll fluorescence using fast repetition rate techniques. I. Defining methodology and experimental protocols. *Biochimica Biophysica Acta* **1367**: 88–106.
- Kvernvik, AC, Hoppe, CJM, Greenacre, M, Verbiest, S, Wiktor, JM, Gabrielsen, TM, Reigstad, M, Leu, E.** 2021. Arctic sea ice algae differ markedly from phytoplankton in their ecophysiological characteristics. *Marine Ecology Progress Series* **666**: 31–55. DOI: <https://doi.org/10.3354/meps13675>.
- Kvernvik, AC, Hoppe, CJM, Lawrenz, E, Prášil, O, Greenacre, M, Wiktor, JM, Leu, E.** 2018. Fast reactivation of photosynthesis in arctic phytoplankton during the polar night. *Journal of Phycology* **54**: 461–470. DOI: <https://doi.org/10.1111/jpy.12750>.
- Kvernvik, AC, Rokitta, SD, Leu, E, Harms, L, Gabrielsen, TM, Rost, B, Hoppe, CJM.** 2020. Higher sensitivity towards light stress and ocean acidification in an Arctic sea-ice-associated diatom compared to a pelagic

- diatom. *New Phytologist* **226**: 1708–1724. DOI: <https://doi.org/10.1111/nph.16501>.
- Lampe, V, Nöthig, E-M, Schartau, M.** 2021. Spatio-temporal variations in community size structure of arctic protist plankton in the Fram Strait. *Frontiers in Marine Science* **7**: 579880. DOI: <https://doi.org/10.3389/fmars.2020.579880>.
- Landry, MR, Calbet, A.** 2004. Microzooplankton production in the oceans. *ICES Journal of Marine Science* **61**(4): 501–507.
- Lavaud, J.** 2007. Fast regulation of photosynthesis in diatoms: Mechanisms, evolution and ecophysiology. *Functional Plant Science and Biotechnology* **1**: 267–287.
- Leu, E, Falk-Petersen, S, Kwaśniewski, S, Wulff, A, Edvardsen, K, Hessen, DO.** 2006. Fatty acid dynamics during the spring bloom in a High Arctic fjord: Importance of abiotic factors versus community changes. *Canadian Journal of Fisheries and Aquatic Sciences* **63**: 2760–2779. DOI: <https://doi.org/10.1139/f06-159>.
- Liu, H, Chen, M, Zhu, F, Harrison, PJ.** 2016. Effect of diatom silica content on copepod grazing, growth and reproduction. *Frontiers in Marine Science* **3**: 89. DOI: <https://doi.org/10.3389/fmars.2016.00089>.
- Llort, J, Lévy, M, Sallée, J-B, Tagliabue, A.** 2015. Onset, intensification, and decline of phytoplankton blooms in the Southern Ocean. *ICES Journal of Marine Science* **72**(6): 1971–1984. DOI: <https://doi.org/10.1093/icesjms/fsv053>.
- MacIntyre, HL, Kana, TM, Geider, RJ.** 2000. The effect of water motion on short-term rates of photosynthesis by marine phytoplankton. *Trends in Plant Science* **5**(1): 12–17.
- Maturilli, M.** 2020a. Basic and other measurements of radiation at station Ny-Ålesund (2006–05 et seq). Alfred Wegener Institute—Research Unit Potsdam, PANGAEA. DOI: <https://doi.org/10.1594/PANGAEA.914927>.
- Maturilli, M.** 2020b. Continuous meteorological observations at station Ny-Ålesund (2011–08 et seq). Alfred Wegener Institute—Research Unit Potsdam, PANGAEA. DOI: <https://doi.org/10.1594/PANGAEA.914979>.
- Maturilli, M, Hanssen-Bauer, I, Neuber, R, Rex, M, Edvardsen, K.** 2019. The atmosphere above Ny-Ålesund: Climate and global warming, ozone and surface UV radiation, in Hop, H, Wiencke, C eds., *The Ecosystem of Kongsfjorden, Svalbard*. (Advances in Polar Ecology, vol 2). Cham, Switzerland: Springer: 23–46.
- Maxwell, K, Johnson, GN.** 2000. Chlorophyll fluorescence—A practical guide. *Journal of Experimental Botany* **51**: 659–668. DOI: <https://doi.org/10.1093/jexbot/51.345.659>.
- McQuoid, MR, Hobson, LA.** 1996. Diatom resting stages. *Journal of Phycology* **32**: 889–902. DOI: <https://doi.org/10.1111/j.0022-3646.1996.00889.x>.
- Nejstgaard, JC, Tang, KW, Steinke, M, Dutz, J, Koski, M, Antajan, E, Long, JD.** 2007. Zooplankton grazing on *Phaeocystis*: A quantitative review and future challenges. *Biogeochemistry* **83**: 147–172. DOI: <https://doi.org/10.1007/s10533-007-9098-y>.
- Nöthig, E-M, Bracher, A, Engel, A, Metfies, K, Niehoff, B, Peeken, I, Bauerfeind, E, Cherkasheva, A, Gäbler-Schwarz, S, Hardge, K, Kilias, E, Kraft, A, Kidane, YM, Lalande, C, Piontek, J, Thomisch, K, Wurst, M.** 2015. Summertime plankton ecology in Fram Strait—A compilation of long- and short-term observations. *Polar Research* **34**: 23349. DOI: <https://doi.org/10.3402/polar.v34.23349>.
- Orkney, A, Platt, T, Narayanaswamy, BE, Kostakis, I, Bouman, HA.** 2020. Bio-optical evidence for increasing *Phaeocystis* dominance in the Barents Sea. *Philosophical Transactions of the Royal Society* **378**: 20190357. DOI: <https://doi.org/10.1098/rsta.2019.0357>.
- Oxborough, K.** 2012. FastPro8 GUI and FRRf3 systems documentation. West Molesey, UK: Chelsea Technologies Group Ltd.
- Pančić, M, Torres Rocio, R, Almeda, R, Kiørboe, T.** 2019. Silicified cell walls as a defensive trait in diatoms. *Philosophical Transactions of the Royal Society B* **286**: 20190184. DOI: <https://doi.org/10.1098/rspb.2019.0184>.
- Paulsen, ML, Riisgaard, K, St. John, M, Thingstad, TF, Nielsen, TG.** 2017. Heterotrophic nanoflagellate grazing facilitates subarctic Atlantic spring bloom development. *Aquatic Microbial Ecology* **78**: 161–176.
- Paulsen, ML, Riisgaard, K, Thingstad, TF, St. John, M, Nielsen, TG.** 2015. Winter-spring transition in the subarctic Atlantic: Microbial response to deep mixing and pre-bloom production. *Aquatic Microbial Ecology* **76**: 49–69.
- Pavlova, O, Gerland, S, Hop, H.** 2019. Changes in sea-ice extent and thickness in Kongsfjorden, Svalbard (2003–2016), in Hop, H, Wiencke, C eds., *The ecosystem of Kongsfjorden, Svalbard*. Cham, Switzerland: Springer: 105–136. (Advances in polar ecology; vol. 2).
- Pierrot, DE, Lewis, E, Wallace, DWR.** 2006. MS Excel Program developed for CO₂ system calculations. ORNL/CDIAC-105a. Carbon Dioxide Information Analysis Centre, Oak Ridge National Laboratory, U.S. Department of Energy.
- Ray, JL, Althammer, J, Skaar, KS, Simonelli, P, Larsen, A, Stoecker, D, Sazhin, A, Ijaz, UZ, Quince, C, Nejstgaard, JC, Frischer, M, Pohnert, G, Troedson, C.** 2016. Metabarcoding and metabolome analyses of copepod grazing reveal feeding preference and linkage to metabolite classes in dynamic microbial plankton communities. *Molecular Ecology* **25**: 5585–5602. DOI: <https://doi.org/10.1111/mec.13844>.
- Reigstad, M, Wassmann, P.** 2007. Does *Phaeocystis* spp. contribute significantly to vertical export of organic carbon? *Biogeochemistry* **83**: 217–234. DOI: <https://doi.org/10.1007/s10533-007-9093-3>.
- Reigstad, M, Wassmann, P, Wexels Riser, C, Øygarden, S, Rey, F.** 2002. Variations in hydrography, nutrients and chlorophyll *a* in the marginal ice-zone and the central

- Barents Sea. *Journal of Marine Systems* **38**: 9–29. DOI: [https://doi.org/10.1016/S0924-7963\(02\)00167-7](https://doi.org/10.1016/S0924-7963(02)00167-7).
- Rokkan Iversen, K, Seuthe, L.** 2011. Seasonal microbial processes in a high-latitude fjord (Kongsfjorden, Svalbard): I. Heterotrophic bacteria, picoplankton and nanoflagellates. *Polar Biology* **34**: 731–749. DOI: <https://doi.org/10.1007/s00300-010-0929-2>.
- Rose, JM, Caron, DA.** 2007. Does low temperature constrain the growth rates of heterotrophic protists? Evidence and implications for algal blooms in cold waters. *Limnology and Oceanography* **52**: 886–895. DOI: <https://doi.org/10.4319/lo.2007.52.2.0886>.
- Rousseau, V, Becquevort, S, Parent, J-Y, Gasparini, S, Daro, M-H, Tackx, M, Lancelot, C.** 2000. Trophic efficiency of the planktonic food web in a coastal ecosystem dominated by *Phaeocystis* colonies. *Journal of Sea Research* **43**: 357–372. DOI: [https://doi.org/10.1016/S1385-1101\(00\)00018-6](https://doi.org/10.1016/S1385-1101(00)00018-6).
- Rousseau, V, Vault, D, Casotti, R, Cariou, V, Lenz, J, Gunkel, J, Baumann, M.** 1994. The life cycle of *Phaeocystis* (Prymnesiophyceae): Evidence and hypotheses. *Journal of Marine Systems* **5**: 23–39. DOI: [https://doi.org/10.1016/0924-7963\(94\)90014-0](https://doi.org/10.1016/0924-7963(94)90014-0).
- Ryderheim, F, Hansen, PJ, Kiørboe, T.** 2022. Predator field and colony morphology determine the defensive benefit of colony formation in marine phytoplankton. *Frontiers in Marine Science* **9**. <https://www.frontiersin.org/articles/10.3389/fmars.2022.829419>.
- Silsbe, GM, Kromkamp, JC.** 2012. Modeling the irradiance dependency of the quantum efficiency of photosynthesis. *Limnology and Oceanography: Methods* **10**: 645–652.
- Singh, A, David, TD, Tripathy, SC, Naik, RK.** 2020. Interplay of regional oceanography and biogeochemistry on phytoplankton bloom development in an Arctic fjord. *Estuarine, Coastal and Shelf Science* **243**: 106916. DOI: <https://doi.org/10.1016/j.ecss.2020.106916>.
- Smetacek, V.** 2001. A watery arms race. *Nature* **411**: 745.
- Smetacek, V, Klaas, C, Strass, VH, Assmy, P, Montresor, M, Cisewski, B, Savoye, N, Webb, A, d'Ovidio, F, Arrieta, JM, Bathmann, U, Bellerby, R, Berg, GM, Croot, P, Gonzalez, S, Henjes, J, Herndl, GJ, Hoffmann, LJ, Leach, H, Losch, M, Mills, MM, Neill, C, Peeken, I, Röttgers, R, Sachs, O, Sauter, E, Schmidt, MM, Schwarz, J, Terbrüggen, A, Wolf-Gladrow, D.** 2012. Deep carbon export from a Southern Ocean iron-fertilized diatom bloom. *Nature* **487**(7407): 313–319. DOI: <http://www.nature.com/nature/journal/v487/n7407/abs/nature11229>.
- Smith, WO Jr, Tozzi, S, Long, MC, Sedwick, PN, Pelouquin, JA, Dunbar, RB, Hutchins, DA, Kolber, Z, DiTullio, GR.** 2013. Spatial and temporal variations in variable fluorescence in the Ross Sea (Antarctica): Oceanographic correlates and bloom dynamics. *Deep Sea Research I: Oceanographic Research Papers* **79**: 141–155. DOI: <http://dx.doi.org/10.1016/j.dsr.2013.05.002>.
- Thompson, R.** 1983. Low-pass filters to suppress inertial and tidal frequencies. *Journal of Physical Oceanography* **13**(6): 1077–1083. DOI: [https://doi.org/10.1175/1520-0485\(1983\)013<1077:LPFTSI>2.0.CO;2](https://doi.org/10.1175/1520-0485(1983)013<1077:LPFTSI>2.0.CO;2).
- Tremblay, J-É, Anderson, LG, Matrai, P, Coupel, P, Bélanger, S, Michel, C, Reigstad, M.** 2015. Global and regional drivers of nutrient supply, primary production and CO₂ drawdown in the changing Arctic Ocean. *Progress in Oceanography* **139**: 171–196. DOI: <https://doi.org/10.1016/j.pocean.2015.08.009>.
- Trimborn, S, Thoms, S, Petrou, K, Kranz, S, Rost, B.** 2014. Photophysiological responses of Southern Ocean phytoplankton to changes in CO₂ concentrations: Short-term versus acclimation effects. *Journal of Experimental Marine Biology and Ecology* **451**: 44–54. DOI: <https://doi.org/10.1016/j.jembe.2013.11.001>.
- Tverberg, V, Skogseth, R, Cottier, F, Sundfjord, A, Walczowski, W, Inall, ME, Falck, E, Pavlova, O, Nilsen, F.** 2019. The Kongsfjorden Transect: Seasonal and inter-annual variability in hydrography, in Hop, H, Wiencke, C eds., *The ecosystem of Kongsfjorden, Svalbard*. Cham, Switzerland: Springer: 49–104. (Advances in polar ecology; vol. 2).
- Vader, A, Marquardt, M, Meshram, AR, Gabrielsen, TM.** 2015. Key Arctic phototrophs are widespread in the polar night. *Polar Biology* **38**: 13–21. DOI: <https://doi.org/10.1007/s00300-014-1570-2>.
- van de Poll, WH, Maat, DS, Fischer, P, Rozema, PD, Daly, OB, Koppelle, S, Visser, RJW, Buma, AGJ.** 2016. Atlantic advection driven changes in glacial meltwater: Effects on phytoplankton chlorophyll-*a* and taxonomic composition in Kongsfjorden, Spitsbergen. *Frontiers in Marine Science* **3**: 200. DOI: <https://doi.org/10.3389/fmars.2016.00200>.
- van de Poll, WH, Maat, DS, Fischer, P, Visser, RJW, Brussaard, CPD, Buma, AGJ.** 2020. Solar radiation and solar radiation driven cycles in warming and freshwater discharge control seasonal and inter-annual phytoplankton chlorophyll *a* and taxonomic composition in a high Arctic fjord (Kongsfjorden, Spitsbergen). *Limnology and Oceanography* **66**: 1221–1236. DOI: <https://doi.org/10.1002/lno.11677>.
- Vaquer-Sunyer, R, Duarte, CM, Santiago, R, Wassmann, P, Reigstad, M.** 2010. Experimental evaluation of planktonic respiration response to warming in the European Arctic Sector. *Polar Biology* **33**: 1661–1671. DOI: <https://doi.org/10.1007/s00300-010-0788-x>.
- von Quillfeldt, CH.** 2000. Common diatom species in Arctic spring blooms: Their distribution and abundance. *Botanica Marina* **43**: 499–516. DOI: <https://doi.org/10.1515/bot.2000.050>.
- Wassmann, P, Ratkova, T, Reigstad, M.** 2005. The contribution of single and colonial cells of *Phaeocystis pouchetii* to spring and summer blooms in the north-eastern North Atlantic. *Harmful Algae* **4**: 823–840. DOI: <https://doi.org/10.1016/j.hal.2004.12.009>.
- Webb, W, Newton, M, Starr, D.** 1974. Carbon dioxide exchange of *Alnus rubra*. *Oecologia* **17**: 281–291. DOI: <https://doi.org/10.1007/bf00345747>.

- White, E, Hoppe, CJM, Rost, B.** 2020. The Arctic picoeukaryote *Micromonas pusilla* benefits from ocean acidification under constant and dynamic light. *Biogeosciences* **17**(3): 635–647. DOI: <https://doi.org/10.5194/bg-17-635-2020>.
- Wiedmann, I, Ceballos-Romero, E, Villa-Alfageme, M, Renner, AHH, Dybwad, C, van der Jagt, H, Svensen, C, Assmy, P, Wiktor, JM, Tatarek, A, Różańska-Pluta, M, Iversen, MH.** 2020. Arctic observations identify phytoplankton community composition as driver of carbon flux attenuation. *Geophysical Research Letters* **47**: e2020GL087465. DOI: <https://doi.org/10.1029/2020GL087465>.
- Willis, K, Cottier, F, Kwasniewski, S, Wold, A, Falk-Petersen, S.** 2006. The influence of advection on zooplankton community composition in an Arctic fjord (Kongsfjorden, Svalbard). *Journal of Marine Systems* **61**: 39–54. DOI: <https://doi.org/10.1016/j.jmarsys.2005.11.013>.
- Wolf, C, Iversen, M, Klaas, C, Metfies, K.** 2016. Limited sinking of *Phaeocystis* during a 12 days sediment trap study. *Molecular Ecology* **25**: 3428–3435. DOI: <https://doi.org/10.1111/mec.13697>.
- Wolf, KKE, Hoppe, CJM, Rost, B.** 2017. Resilience by diversity: Large intraspecific differences in climate change responses of an Arctic diatom. *Limnology and Oceanography* **63**: 397–411. DOI: <https://doi.org/10.1002/lno.10639>.
- Xing, X, Claustre, H, Blain, S, D'Ortenzio, F, Antoine, D, Ras, J, Guinet, C.** 2012. Quenching correction for in vivo chlorophyll fluorescence acquired by autonomous platforms: A case study with instrumented elephant seals in the Kerguelen region (Southern Ocean). *Limnology and Oceanography: Methods* **10**: 483–495. DOI: <https://doi.org/10.4319/lom.2012.10.483>.
- Zhang, S, Liu, H, Ke, Y, Li, B.** 2017. Effect of the silica content of diatoms on protozoan grazing. *Frontiers in Marine Science* **4**: 202. DOI: <https://doi.org/10.3389/fmars.2017.00202>.

How to cite this article: Hoppe, CJM, Wolf, KKE, Cottier, F, Leu, E, Maturilli, M, Rost, B. 2024. The effects of biomass depth distribution on phytoplankton spring bloom dynamics and composition in an Arctic fjord. *Elementa: Science of the Anthropocene* 12(1). DOI: <https://doi.org/10.1525/elementa.2023.00137>

Domain Editor-in-Chief: Jody W. Deming, University of Washington, Seattle, WA, USA

Associate Editor: Mathieu Ardyna, Takuvik International Research Laboratory, CNRS/Université Laval, Québec City, Canada

Knowledge Domain: Ocean Science

Published: December 10, 2024 **Accepted:** October 23, 2024 **Submitted:** December 06, 2023

Copyright: © 2024 The Author(s). This is an open-access article distributed under the terms of the Creative Commons Attribution 4.0 International License (CC-BY 4.0), which permits unrestricted use, distribution, and reproduction in any medium, provided the original author and source are credited. See <http://creativecommons.org/licenses/by/4.0/>.